An edited version of this paper was published in *Journal of Hydrology (doi:* 10.1016/j.jhydrol.2016.05.008)

The influence of flow inertia, buoyancy, wind, and flow unsteadiness on mixing at the asymmetrical confluence of two large rivers

Cintia L. Ramón [(1)(a)(*)], Jordi Prats[(2,3)(b,c)], and Francisco J. Rueda [(1)(d)]

[(1)] Water Research Institute and Department of Civil Engineering, University of Granada. C/Ramón y Cajal, 4 - 18003 Granada, Spain. ([a]crcasanas@ugr.es, [d]fjrueda@ugr.es).

[(2)] Flumen Institute, Technical University of Catalonia. C/Jordi Girona 1-3 Edifici D1-2a planta, -08034, Barcelona, Spain ([b] jordi.prats-rodriguez@upc.edu).

[(3)] National Research Institute of Science and Technology for Environment and Agriculture (IRSTEA) 3275 Cézanne Rd., CS 40061 Aix-en-Provence Cedex 5, 13182, France. ([c]jordi.prats@irstea.fr)

[(*)] Corresponding author

Abstract

The rates and patterns of mixing of two large rivers with large density differences at a strongly asymmetrical confluence in northern Spain are analyzed. We assess the factors controlling the site where the denser river plunges and the mixing rates between the rivers. In particular, we focus on the interaction between inertial and buoyancy forces, the effect of wind forcing, and the unsteady nature of the hydraulic forcing. The steady-state location of the plunge line is shown to be controlled by an inertia-buoyancy balance, which accounts for the relative magnitude of the buoyancy forcing associated with density differences between the confluent rivers, and the magnitudes of both the main-stream and the side-flow (tributary) inertia. The plunge line moves to upstream locations as the inertia of the tributary increases (for low tributary inertia) and/or the density contrast between the rivers increases. This has important consequences for river mixing since mixing rates increase as the plunging occurs at the confluence. The high mixing rates in this case occur as a result of a large mixing interface surface area and high diffusivities. As the plunging area moves upstream or downstream of the confluence, vertical diffusivities or the area of contact available for mixing decrease and constrain mixing rates. Wind forcing, depending on its velocity and direction, affects mixing rates through (1) altering the buoyancy-inertia equilibrium and so changing the location of the plunge line, (2) altering the pattern of secondary circulation within the confluence and/or (3) increasing shear at the confluence. Flow unsteadiness can lead to changes in the location of the plunge line through time and thus can strongly modify mixing rates at the confluence. The downstream movement of the plunge line is advection dominated, while its upstream movement seems to respond to a baroclinic response of the confluence.

Keywords

River mixing; stratification; plunge point; shear; wind forcing

1. Introduction

The strongest physical and chemical gradients in river networks occur in confluences, where two rivers draining different watersheds merge (Bigelow et al., 2007; Gooseff et al., 2008; Kiffney et al., 2006). A wide range of environmental conditions for growth occur at those sites, leading to species-rich biological communities, with a number of species that tends to be larger than elsewhere in the river network (Benda et al., 2004; Rice et al., 2006). The persistence downstream of heterogeneous habitat conditions largely depends on the rate of mixing between the confluent flows and on the spatial arrangement of the flows at and downstream of the confluence, that is, whether rivers flow side by side or on top of the other. Water from the two confluent rivers will flow side by side if their densities are similar and the rate at which they mix will largely depend on the extent to which the nearly-vertical mixing layer that develops between the confluent rivers distorts, increasing the area of contact between water masses. The distortion of the mixing layer, in turn, may occur as a result of differences in depths between the main channel and the tributary (bed discordance) or channel-scale helical motions, which in general result in significant reductions in mixing lengths (e.g., Gaudet and Roy, 1995; Lane et al., 2008; Rhoads and Kenworthy, 1995). The development of two dimensional vortices in the shear layer between the confluent rivers has also been shown to increase mixing rates between the water masses but their effect on river mixing could be rather limited (Konsoer and Rhoads, 2014; Lane et al., 2008). Very recently Ramón et al. (2014) also argued that weak density differences between the confluent rivers may lead to larger distortion rates of the mixing interface, producing larger contact areas between the rivers and enhancing mixing rates.

Most studies published in the literature on river confluences have been conducted under homogeneous or weakly stratified conditions. Few studies, however, have focused on confluences of rivers with strong density contrasts. Under those conditions, the denser river will plunge and flow below the less dense river and the interface separating the confluent rivers will tend to become nearly horizontal downstream of the plunge point (Cook et al., 2006; Lyubimova et al., 2014; Ramón et al., 2013).

Lyubimova et al. (2014) further observed that the position of the water surface where the denser flow actually plunges (plunge point) could be upstream of the confluence under strongly buoyant conditions and low flow rates along the main river. The behavior of plunging flows has been thoroughly studied in long, narrow, straight and quiescent basins with simple geometries, using laboratory experiments (e.g., Cortés et al., 2014; Wells and Nadarajah, 2009, and references therein), numerical simulations (e.g., Bournet et al., 1999; Chung and Gu, 1998; Kassem et al., 2003), and analysis of field data (e.g., Arneborg et al., 2007; Dallimore et al., 2001; Fischer and Smith, 1983). The behavior of the buoyant river inflows can be interpreted as the interplay between the inertia of the river inflow and buoyancy forces, associated with the density differences between the inflow and the stagnant water in the basin. Hence, it can be parameterized in terms of the internal Froude number, $Fr_i = u/(g'D)^{1/2}$ where, u represents the inflow velocity, D the depth of the channel and $g' = g\ \Delta\rho/\rho_0$, the reduced gravity calculated from the density differences between lake and river water and a reference density ρ_0. Upstream of the plunge/lift point it is assumed that motion is dominated by inertial forces and $Fr_i >> 1$. Downstream, in turn, buoyancy forces dominate the motion and $Fr_i << 1$. At the plunge/lift point Fr_i is O (1), and most expressions proposed to determine the location of the plunge/lift points are based on this condition. Similar arguments can be used to analyze the behavior of confluent rivers with strong buoyancy differences. Side-flow inertia and the basin geometry, however, need to be also taken into account in determining the site of the plunging and the shape of the mixing interface in river confluences. The role of side-flow inertia and, in general, the behavior of river confluences under strong density contrasts have not been studied in detail before in the literature.

Our general goal is to understand the factors that control the spatial arrangement of water masses and mixing rates across the contact interface in river confluences under strong density contrasts. To that end, we conduct simulations of hydrodynamic and transport processes occurring in a confluence in Northern Spain where the Ebro (hereon, Western W- or main river) and Segre rivers (Northern N-River or tributary) merge with a strong asymmetry, i.e., a nearly 90º junction angle (Ramón et al., 2013). The flow rates along the main river are regulated by a dam constructed approximately 2.5 km upstream of the junction apex (Fig. 1a), which could result in high fluctuations in the W-inflow rates throughout the day, following hydro-power generation rules (e.g., Figs. 1b-c). The W-River is denser than the N-River during most times of the year (up to 63% of the time in the stratification period, from June to November, and 79% when considering the whole year, based on the analysis of available historical data). Hence, here we focus on the analysis of the spatial arrangement of the rivers when the main river is denser than the tributary. We hypothesize that the mixing rates and the spatial arrangement of the two rivers at the confluence under steady forcing, whether the confluence appears stratified or not, depends on whether the denser main river plunges upstream or downstream of the confluence. This, in turn, is controlled by (1) the ratio of inertial forces between the confluent rivers, which can be parameterized in terms of the ratio between the tributary to the main velocities $R_u = u_N/u_W$, and (2) the ratio of the buoyancy of the tributary and the magnitude of the inertial forces along the main channel, which can be parameterized in terms of a confluence internal Froude number $Fr_{ic} = u_W/(g'D)^{0.5}$. Here, u_N and u_W are the inflow velocities in the tributary and the main stream, respectively, and the reduced gravity g' ($g' = g\,(\rho_W - \rho_N)/\rho_0 = g\,\Delta\rho/\rho_0$) is calculated from the density difference between the two rivers and a reference density ρ_0 ($\rho_0 = 1000$ kg m^{-3}). Although the discharge ratio R_q ($R_q = Q_N/Q_W$) and the momentum flux ratio R_m ($R_m = [u_N\ Q_N\ \rho_N] / [u_W\ Q_W\ \rho_W]$) are commonly used as a metric for the bulk inertial forces of confluent flows, in this study R_u corresponds directly (same order of magnitude) to R_q, and it was chosen over R_q to be consistent with the parameterization of inertial forces given by the Froude number. Other factors that may control the spatial arrangement and, hence, mixing rates observed at a given time at the confluence include: the time-varying nature of the inflow rates along the main river and wind forcing. In their analysis of data from their field experiments, Ramón et al. (2013) suggested that the strong southeasterly winds that blew during the stratification period were playing an important role in the spatial arrangement of the W- and N-rivers at their confluence. To our knowledge, these effects have not been analyzed previously in the literature.

2. Study site

Ribarroja reservoir (41º18' N, 0º21' E) is the second of a chain of three reservoirs (Mequinenza-Ribarroja-Flix) constructed along the lower reaches of the W-River for hydroelectric power generation. The reservoir has an elongated and meandering shape (Fig. 1a), with an average depth of 9.8 m, reaching values of up to 34 m near the dam. The system is strongly regulated via inflows and outflows so that the free surface elevation is kept at a nearly constant value of approximately 69 m above sea level throughout the year. The residence time of the water in the reservoir is low and never exceeds one month even during the lowest through-flows typically observed in summer (Cruzado et al., 2002). The two largest inflows to the reservoir are the W- and N- rivers, which merge at a near 90º junction angle at the NW end of the reservoir. The confluence is characterized by its curved planform which bends to the left with a radius of curvature R_s of ≈ 3 km, almost 7 times the post-confluence channel width b_p ≈ 400 m,

$R_s/b_p \approx 7.5$ (Fig. 1a). Depths of the W- and N- rivers are discordant: the N-River enters the confluence through two channels of depths D of 4 m and 2 m, respectively, while depths encountered at the W-River are of O (10) m.

3. Methods

3.1 Computational model

Simulations were conducted using a parallel version (Acosta et al., 2010) of a three-dimensional primitive-equation (3D-PE) model that solves the layer-averaged form of the shallow water equations (Smith, 2006). The momentum equations are solved on a staggered Cartesian grid, using an efficient second-order accurate, space-centered, semi-implicit and three-level iterative leapfrog-trapezoidal finite difference scheme. Non-active- (i.e., tracers) and active-scalar transport equations were solved using a two-level semi-implicit scheme, in which only vertical diffusion is discretized implicitly. The advection terms in the transport equation for active and non-active scalars are discretized with a second-order accurate flux-limiting scheme (e.g., Durran, 1999). Turbulent mixing is represented in the 3D-PE model using diffusion-like terms. A Laplacian operator with constant mixing coefficients K_h is used to represent the unresolved horizontal turbulent mixing of momentum and scalars. Vertical eddy coefficients of mixing K_z are calculated using a two-equation model originally proposed by Mellor and Yamada (1974) and later modified by Kantha and Clayson (1994). This turbulent modeling approach is typically used in large scale models of river and estuarine flows (e.g., Chua and Fringer, 2011; Gleichauf et al., 2014; Morillo et al., 2008; Wang et al., 2011; Wolfram et al., 2016) given the large aspect ratios of their grids and its reduced computational burden. The present implementation of the model follows the formulation of Gross et al. (1999), which considers vertical diffusion as the only form of transport.

Our modeling approach is further justified given the need to conduct unsteady simulations of time-varying inflow rates during the stratification period (Ramón et al., 2013) in a large domain with a reasonable computational cost. Our simulations with a 10-m-resolution grid require O (10^5) computational time steps, which limits the use of full 3D RANS models based on non-hydrostatic equations or the use of more sophisticated modeling approaches such as well-resolved Large Eddy Simulations (LES) (Rodi, 2010) or even the hybrid Reynolds-Averaged Navier Stokes (RANS)-LES approach of (Constantinescu et al., 2012, 2011). The model has been extensively validated both against analytical solutions and field data sets collected in a variety of lake environments (Rueda and MacIntyre, 2010, and references therein) and estuaries (Llebot et al., 2014), and for relevant physical processes occurring in river confluences, including (1) the development of a shallow mixing layer between two confluent streams, (2) flow past a cavity, and (3) flow in open channels of mild curvature with and without stratification (Ramón et al., 2015). Additional tests (e.g., Appendix A) were conducted to check the ability of the model to represent Kelvin Helmholtz instabilities. These additional tests included simulations of the shallow mixing layers reported by Chu and Babarutsi (1988) and Uijttewaal and Booij (2000). Ramón et al. (2015) also validated the model results (runs U1-3, Table 1) against field data collected at the confluence.

3.2 Approach

The model was first used to evaluate our hypothesis of an inertia-buoyancy balance at the Ebro-Segre confluence. A first set of simulations (A-series in Table 1) were conducted under steady hydraulic and buoyancy forcing. The forcing conditions correspond to a range of values for the river velocity ratio R_u and confluence internal Froude number Fr_{ic} that can potentially occur at the confluence during the stratification period (Fig. 2). Modeled velocities were then applied to simulate the transport of a tracer injected in the domain through the W-River. The time-averaged spatial arrangement of the confluent rivers, the location of the plunge line (the region at surface where the denser W-River plunges below the N-River) and mixing rates were analyzed. A subset of the simulations included in the A-series corresponds to the daily-averaged forcing conditions observed under stratified conditions in 2009 (Ramón et al., 2013). This subset is referred to as S-runs in Table 1. These simulations were re-run but subject, this time, to different wind speeds and directions (SW-runs in Table 1), to analyze the interaction of wind forcing, R_u and Fr_{ic} in determining the spatial arrangement of the rivers and their mixing rates at the confluence. A final set of simulations was conducted subject to the time varying flow rates and wind forcing (U-runs in Table 1) observed in 2009 (Ramón et al., 2013) (Figs. 1b-g). The results of these runs focus on the effect of unsteadiness in the hydraulic forcing on the relevant time scales of response (location of the plunge point) of the system.

3.3 Transport and mixing model of the Ribarroja reservoir

Our computational domain extends from Mequinenza dam to a section approximately 8 km downstream of the junction apex (shaded gray area in Fig. 1a) along the W-River, and approximately 500 m upstream of the confluence along the N-River. Our study area, however, is shorter and extends only 2.3 km downstream of the junction apex (Fig. 1a). The N-boundary was placed 1 km upstream of the confluence. The lake geometry was discretized using grid cells of size (Δx, Δy, Δz) = (10, 10, 0.5) meters in the longitudinal, lateral and vertical direction, respectively. For stability purposes, the time step Δt was set to 3 s in all but in the SW- runs, for which Δt = 2 s. The bottom drag coefficient, C_d, was set to 0.003 as proposed by Smith (2006). The reservoir was assumed initially at rest with a uniform density, equal to the averaged density of the W- and N- rivers. At the downstream end, the free surface elevation was fixed, with densities and tracer concentrations having zero gradients. Inflow rates at the upstream boundaries, in turn, were changed depending on the simulation series, and either set to conform to the field data of Ramón et al. (2013), or to constant values representing a range of density and momentum conditions. N-inflows were assumed to occur through two sections (Fig. 1a) with different velocities, as observed in the field. Almost 2/3 of the total inflow rate from the N-River was presumed to enter through the main channel and the remaining through the secondary channel. Inflow rates in the W-River were distributed uniformly in the inflow section. All inflow densities were set to be constant in time (Table 1).

The model was set to run using two trapezoidal iterations after the initial non-smoothed leapfrog predictive step. The superbee limiter (Roe, 1984) was used in the solution of the scalar transport equation. Other flux-limiters tested (van Leer, 1974) yielded similar results. With approximately 40 grid cells across the channel, and almost 20 cells in depth, mixing and dispersive processes scaling with the channel dimensions are well resolved, and the sub-grid scale mixing to parameterize is mainly the turbulent diffusion. Based on a large set of experiments in rivers, Fischer et al. (1979) argued that the non-dimensional transverse mixing coefficient $\varepsilon_t/Du^* = K_h/ Du^*$ should be approximately 0.15 with an error bound of ± 50%, u^* being the shear velocity ($u^* = u_s C_d^{0.5}$). For average post-confluence streamwise velocities u_s ranging from 0.03 to 0.45 m s^{-1}, as encountered in the simulations and D = 10 m, K_h could range from O (10^{-3}) to

O (10^{-2}) m^2 s^{-1}. Even lower values of O (10^{-4}) m^2 s^{-1} and zero were used by Wang et al. (2011) or Chua and Fringer (2011) in their simulations of the Snohomish River estuary, and North San Francisco Bay, respectively, and justified based on the high numerical diffusion of their advective scheme. In our simulations, with a non-diffusive advective algorithm, the horizontal mixing coefficient K_h was still set to 10^{-5} m^2 s^{-1}, but additional runs were conducted with K_h up to 10^{-1} m^2 s^{-1} to check the sensitivity of our results to this parameter.

Given that the 3D-PE model is hydrostatic, and, being the grid aspect ratio $\Delta z/\Delta x$ of O (10^{-2}), hence, $\Delta z/\Delta x << 1$, non-hydrostatic flow features will not be resolved. The importance of the non-hydrostatic pressure effects in a given flow can be assessed, as pointed by Wang et al. (2009), by considering the ratio δ of the scales for the vertical and horizontal variability of the flow. For features with $\delta \approx$ O (1), those effects are significant and should not be neglected. For those with $\delta^2 << 1$, non-hydrostatic effects can be safely ignored. The latter is the case of the secondary circulation that develops at the confluence, which has length scales ranging from ~125 m to the channel width b_p and a vertical scale equal to the depth of the channel D, and for which δ^2 is of O (10^{-3}-10^{-4}), i.e., $\delta^2 << 1$. The role of these largely-hydrostatic features in controlling river mixing in confluences is well documented in the literature (see, for example, Rhoads and Kenworthy, 1998, 1995; Rhoads and Sukhodolov, 2001). The influence of non-hydrostatic flow phenomena, in turn, remains largely unexplored, and an open question. Hence, the 3D-PE model should provide, at least to first order, a reasonable representation of flow and mixing in the confluence.

A total of 74 simulations were run in the A-series (Table 1), with values of R_u and Fr_{ic} encompassing conditions observed at the confluence under the stratified conditions in 2009 (Ramón et al., 2013) and other years (Fig. 2). River density contrasts

$\Delta\rho/\rho_0$ were set equal to those observed in 2009 (Ramón et al., 2013) and river inflow rates were varied to achieve different values for R_u and Fr_{ic}. For the Fr_{ic} calculations the average depth of the W-River (D = 10 m) was used. Only for the simulations with the lowest Fr_{ic} (≤ 0.08), a fictitious river density contrast of 4.7×10^{-3} was used. In all A-simulations, the density contrast was assumed driven by temperature differences alone.

The particular forcing conditions observed on days 203, 329 and 330 in 2009 (Ramón et al., 2013) were used to develop boundary and initial conditions for the S-, SW-, and U-runs (Figs. 1b-g, Table 1). The confluence was then stratified, and density contrasts between the rivers were driven by both differences in temperature and salinity/conductivity. On day 203, the density difference was O (10^{-3}) and on days 329 and 330, in turn, $\Delta\rho/\rho_0$ was O (10^{-4}). Inflow rates from the N-River, Q_N, were constant but those from the W-River, Q_W, were variable (Figs. 1b-c). The daily-averaged R_q, R_u, R_m and Fr_{ic} values on days 203, 329 and 330 are shown in Table 1. Winds were moderate in November, but strong, with average speeds of 7 m s^{-1} (Fig. 1d), and from the SSE-SE on day 203 (Fig. 1f). In the S-simulations (runs S1-3 in Table 1) the model was forced using the observed daily-average inflow rates and the observed density differences, until reaching steady-state. In the SW-runs (runs SW1-SW20 in Table1), the steady-state simulations on days 203 and 329 were forced with different, but constant, wind speeds U_{10} and directions Φ. A total of 20 simulations were conducted in which we tested the dominant wind direction, as observed in 2009 (southeasterly winds, $\approx 135^{\circ}$, Fig. 1h), together with 4 ideal winds blowing from each of the four cardinal directions. We also tested two wind speeds: U_{10} = 6 m s^{-1}, which correspond to the 85 percentile of wind velocities in 2009, and U_{10} = 12 m s^{-1}, the largest magnitude observed in 2009 (Fig. 1h). Finally, in the U-series of simulations (runs U1-U3 in Table

1), the model was run subject to unsteady W-inflow rates and wind forcing as observed on days 203, 329 and 330 in 2009.

In any given simulation, the model was run with the same inflow and outflow conditions day after day until at least 99% of the water mass initially existing in the domain had left the computational domain. This length of time was 7 days, on average, and always less than 20 days for the flow rates tested.

3.4 Tracer experiments, mixing rates and plunging point

W-water was traced using a constant tracer concentration C_W = 100 ppm. Tracer concentrations downstream, varying from 0 to 100, indicated the percentage of W-water in the mixture, and hence, were used to establish the level of mixing between the W- and N- rivers. Tracer variability was evaluated each 0.25 hours at 16 cross-sections downstream of the confluence (cross-sections B1-B16, Fig. 1a). The distance between consecutive B-sections was approximately 120 m. Tracer variability was also evaluated at 43 sections in the W-channel (cross-sections W1-W43, Fig. 1a), which are approximately 55 m apart, and at 6 sections within the confluence region (cross-sections A1-A6, Fig. 1a). We will use the symbol x_c to refer to the distance downstream of the junction apex of each of these cross-sections (W-sections will take negative values), and will be given as a multiple of b_p. We used the standard deviation σ of tracer concentration (Biron et al., 2004; Ramón et al., 2014) to quantify mixing levels. Standard deviations will tend to decrease downstream of the confluence as a result of mixing (Fig. 3), and they will become zero when tracer concentrations are uniform in a given cross-section. By contrast, standard deviations > 0 ppm upstream of the confluence in the W-channel, indicate the presence of N-water in the W-channel (Fig. 3). To compare mixing among simulations and different days, mixing rates, calculated as $\Delta\sigma/s = (\sigma_i - \sigma_0)/s_i$, and total mixing, calculated as $TM = (1 - \sigma_i/\sigma_0) \times 100$, were evaluated at section i = B16 (Fig. 1a). Here, s_i and σ_i are the distance downstream of the junction apex and the standard deviation of tracer concentrations at B16, respectively. The expected standard deviation of tracer concentrations if no mixing occurs between the two rivers, is represented by σ_0, and is calculated from the flow rates and tracer concentrations in each of the rivers similarly to Lewis and Rhoads (2015):

$$\sigma_0 = \left(\frac{Q_W (C_W - C_p)^2 + Q_N (C_N - C_p)^2}{Q_W + Q_N} \right)^{0.5}, \qquad (1)$$

where C_p is the theoretical concentration after complete mixing (Gaudet and Roy, 1995), calculated with the daily-averaged inflow rates as:

$$C_p = \frac{C_N Q_N + C_W Q_W}{Q_N + Q_W} \qquad (2)$$

For example, for the values of input tracer concentrations and the daily-averaged inflows used in the model in the S-runs, C_p = 60.13, 73.02 and 58.4 ppm and σ_0 = 48.96, 44.36 and 49.27 ppm on days 203, 329 and 330, respectively. The mixing interface was defined as the set of cells where tracer concentration equals $C_p \pm 10\%$. Cells with $C > C_p + 10\%$ will be representative of the W-water while cells with $C < C_p - 10\%$ will be representative of the N-water (Gaudet and Roy, 1995). Plunging is assumed complete once the maximum surface concentration at any given point in a cross-section is $< C_p +$

10%. The distance from the junction apex to this section will be taken as representing the location of the plunge point $x_{c\text{-}PL}$. The plunge line is identified as the group of surface cells where tracer concentrations transition from C ≥ C_p + 10% to C < C_p + 10%.

4. Results and Discussion

4.1 *Plunging and stratification at the confluence*

The location of the plunge point is represented in Fig. 4 (white isolines) for the different values of R_u and Fr_{ic} shown in Table 1. For the range of R_u values analyzed, there exists a critical Fr_{ic} value ($Fr_{ic} \approx 0.3$), above which the location of the plunge line is always downstream of the junction apex. For $Fr_{ic} > 0.3$, independently of R_u, buoyancy forces associated with the density differences between the rivers are not strong enough to overcome the inertia of the main stream flow and plunging occurs downstream of the junction apex ($x_{c\text{-}PL} > 0$). For $Fr_{ic} \approx 0.9$ and larger the W-River plunges downstream of the confluence ($x_{c\text{-}PL} > 1.76$). The exact location of the plunge point downstream of the junction apex depends, though, on both R_u and Fr_{ic}. Note, for example, that the plunge point is at the center of the confluence ($x_{c\text{-}PL} = 0.93$) for $R_u \approx 0.5$ and $Fr_{ic} \approx 0.7$. As R_u becomes < 0.5 or > 0.5, the plunge point will only remain at the center of the confluence if Fr_{ic} falls below 0.7 (note that the isoline $x_{c\text{-}PL} = 0.93$ deviates from the vertical black line, marking $Fr_{ic} \approx 0.7$, for values of $0.5 < R_u < 0.5$ in Fig. 4). Thus, for $Fr_{ic} > 0.3$, the plunge point forms at the most upstream location for R_u of 0.5 and it is displaced downstream as R_u increases or decreases from that value (Figs. 5a-d).

The tendency of the plunge point to move downstream for $R_u \ll 1$ for a given Fr_{ic} (> 0.3) can be explained in terms of inertial and buoyancy effects at the confluence.

As reported earlier in the literature (e.g., Biron et al., 1993; Rhoads and Kenworthy, 1998, 1995) for neutrally buoyant conditions, the location of the mixing layer moves farther away from the tributary bank as inertial forces in the tributary increase. This is consistent with the location of the mixing layer moving closer to the W-bank as R_u increased from, for example, ≈ 0.15 to ≈ 0.5 for Fr_{ic} ≈ 0.7. By adding a density difference, buoyancy effects sum up to this inertial effect, which allows water from the tributary to reach the opposite bank faster (the plunge point moves upstream) as R_u increases. However, as inertial forces in the tributary keep increasing ($R_u >> 1$ and $R_m >> 1$), inertial effects start controlling the location and orientation of the mixing interface. As tributary inertia increases, the increasing rates of turbulent diffusion will tend to keep the tributary flow attached to bed, counteracting buoyancy effects. This tendency results in a shift in the orientation of the mixing interface towards more vertical positions (e.g., Fig. 5b-d), and thus, in a downstream displacement of the plunge point in Fig. 4 as R_u increases.

As the mixing layer shifts towards more vertical positions for $R_u >> 1$, lateral shear along this interface increases, and as a result, flow structures similar to Kelvin-Helmholtz (KH) instabilities develop (Fig. 6) , which, may contribute to increased lateral mixing. The occurrence of strong KH structures for both $R_m >> 1$ and $R_m << 1$ is consistent with simulations of other river confluences (Constantinescu et al., 2012, 2011). It is also consistent with the work of Prats et al. (2013), based on the analysis of airborne thermal images, which provided evidence of the occurrence of KH-instabilities in the confluence, under $R_u = 0.28$ ($R_m = 0.05$) and $Fr_{ic} = 1.26$. These conditions are among those simulated to produce Fig. 4. In those simulations (not shown), the scales and position of the oscillations in the shear layer were similar to those reported by Prats et al. (2013).

4.2 *Mixing rates*

River mixing varied with both R_u and Fr_{ic} as shown in Fig. 4. For any given R_u, Froude numbers for which mixing rates were maximal ($0.6 < Fr_{ic} < 0.8$) tended to coincide with those for which plunging occurred within the downstream half of the confluence ($0.93 < x_{c\text{-}PL} < 1.76$, see the dashed black line in Fig. 4). Mixing rates decreased away from that range. For $R_u \approx 1$, as Fr_{ic} decreased from O (1) to O (10^{-1}), TM dropped from ≈ 60% to 30%. Those changes are largely the result of the increasing density contrasts between the rivers inhibiting vertical mixing across the mixing interface (see Fig. 7). In the transition of Fr_{ic} from O (1) to O (10^{-1}), the mixing interface between the rivers tended to become horizontal (Figs. 7d-a). The area available for horizontal mixing S_h decreased from O (10^4) to O (10^3) m^2 (Fig. 7e). The area of the mixing interface available for vertical mixing S_z, in turn, increased almost one order of magnitude, from O (10^4) to O (10^5) m^2 (Figs. 7f). But the vertical diffusivities K_z within the mixing layer decreased almost two orders of magnitude from O (10^{-3}) $m^2\,s^{-1}$ to nearly molecular values of O (10^{-5}) $m^2\,s^{-1}$ (Fig. 7g), as typically reported in stratified flow such as estuarine environments (e.g., Lung and O'Connor, 1984).

For $R_u \approx 1$, as Fr_{ic} increased above 0.8, river mixing decreased again (Fig. 4). The mixing interface in those cases tilts and becomes more vertical and aligned with the axis of the main channel for the largest Fr_{ic} tested (Fig. 7c-d). The vertical diffusivities K_z remained constant and of O (10^{-3}) $m^2\,s^{-1}$ (Fig. 7g). The area for horizontal mixing S_h remained similar as Fr_{ic} increased above 0.8 (Figs.7e). The area for vertical mixing S_z and the total area of the mixing interface decreased (Fig. 7f). Hence, maximal mixing rates occur if plunging occurs at the confluence. If it occurs upstream, river mixing tends to decrease as a result of lower vertical diffusivities. If it occurs downstream, in turn, total mixing decreases as a result of reductions in the areas available for mixing. Mixing rates between rivers, hence, are subject to seasonal changes resulting from changes in the position of the plunge point. On day 203, when the plunge line under steady state was located upstream of the confluence (Fig. 4 and Ramón et al. (2013)), mixing rates were O (10^{-3}) ppm m^{-1} (and $TM \approx 29\%$), one order of magnitude lower than mixing rates on days 329 and 330 ($TM > 50\%$) (runs S1-3 in Table 2), when the plunge line was located at the confluence region.

For any given value of the Froude number, Fr_{ic}, total mixing was minimal for R_u of ≈ O (1), increasing both as R_u becomes larger or lower than O (1). Larger mixing rates for larger velocity ratios ($R_u >> 1$) could be the result of high tributary inertia leading to wide and nearly vertical mixing interfaces where KH structures develop (e.g., Fig. 5d and Fig. 6). Mixing in those cases is energetic, with *TM* being larger than 70% for $R_u >> 1$ and all Fr_{ic} tested (Fig. 4). Note that, the mixing layer in Fig. 5d even attached to the W-bank within the study reach. However, *TM* also increased with R_u in our simulations with $K_h = 10^{-1}$ m^2 s, for which KH billows are inhibited, which suggests that another mechanisms could be at play. Past work has shown that the secondary circulation at river confluences typically consists of two counter-rotating cells, which converge near the surface towards the mixing layer and diverge towards the river banks near the bed (e.g., Ashmore et al., 1992; Rhoads and Kenworthy, 1998, 1995). Depending on factors such as the momentum ratio, the junction planform or the junction angle (Bradbrook et al., 2000; Rhoads and Kenworthy, 1998), one of the cells can dominate over the other and even occupy the whole channel. Lewis and Rhoads (2015) argued that mixing rates could increase with R_m as the result of the increasing dominance of the tributary cell. In the A-series, for $Fr_{ic} = 0.45$, for example, the high junction angle together with a positively buoyant tributary produces a secondary circulation which is already dominated by the tributary cell at the confluence, even for the lowest R_u (R_m) tested. As R_u (R_m) increases the strength of the secondary circulation also increases, which is parameterized in Fig. 5h as the Root Mean Square of the width-averaged secondary velocity $u_{n\text{-}rms}$ in section A5 (Fig. 1a). The secondary velocity was calculated with the Rozovskii method (Parsons et al., 2013; Rozovskii, 1961). An increase in the strength of the secondary circulation at the confluence could be responsible for an increase in river mixing as $R_u >> 1$.

The larger mixing rates observed for lower velocity ratios as $R_u << 1$ (see *TM* values for $R_u < 0.4$ and $0.3 < Fr_{ic} < 1.2$ in Fig. 4) are likely the results of the limited vertical extent of the upper layer carrying N-water at the confluence under those conditions. As the velocity ratio decreases, the discharge ratio, and hence, the thickness of the N-layer in the water column also decreases. The distance downstream of the confluence where a layer of limited extent initially occupying the top of the water column becomes fully mixed L_z can be estimated as $L_z = u_s \times d^2/K_z$, in terms of the average streamwise velocity u_s, vertical diffusivity K_z and the layer depth d (e.g., Rutherford, 1994). The streamwise velocity at the confluence for $R_u << 1$ is largely dictated by the inflow velocity of the main river u_W. For $R_u << 1$, K_z also remained almost unchanged (see Fig. 5g for $R_u < 0.61$). Hence, L_z decreased as discharge ratios decreased, and hence, as the thickness of the N-layer decreased, leading to higher *TM*s for the lowest R_u analyzed.

4. 3 *Wind driven changes*

The mechanical energy introduced in the water column by wind forcing acting on the air-water interface alters the large-scale flow field and the turbulent kinetic energy TKE balance, hence, changing mixing rates and the spatial arrangement of the river masses at the confluence. This effect, in turn, is likely to vary depending on the wind direction. Although the winds in Ribarroja are predominantly from the South-East and against the flow in the W-River (Fig. 1a), here, and for the sake of completeness, we analyze the effect of wind forcing, in the four cardinal directions. We further consider two different scenarios with the hydraulic conditions prevailing on days 203 and 329, with strong and moderate buoyancy differences between the rivers. The changes in the TKE balance introduced by winds are either the result of increasing fluxes of TKE across the air-water interface, redistributed in the water column through turbulent diffusion, or, alternatively, the result of the increasing magnitude of vertical shear leading to the local production of TKE within the water column. These two mechanisms of production of TKE are referred to as stirring (P_{sk}) and shear production (P_s). These two terms are balanced by the sinks of TKE, which include frictional dissipation and, in the case of stratified water columns, buoyant dissipation (see Gross et al., 1999, for example). Both the energy available in the system through stirring and shear increased in response to wind forcing (see ratios $R_{sk\text{-}sk0}$ and $R_{s\text{-}s0}$ for the SW-runs in Table 2 which represent percentages with respect to the P_{sk} and P_s values in the S-runs). However, P_{sk} represented always less than 30% of P_s (see ratios *Rsk-s* in Table 2), which suggests that wind forcing increases mixing at the confluence mainly through shear. Hence, the shear production term is taken as a proxy for the effect of wind on the mixing rates.

The easterly winds tended to decelerate the flow along the main river, producing a similar effect as if decreasing Fr_{ic} and increasing R_u relative to the reference values with no winds. As a result of the weaker inertial forces along the channel compared to the buoyancy differences, the plunge point tended to move upstream (see $x_{c\text{-}PL}$ values in Table 2 for S1 and SW2). Note that in Fig. 8a, the plunge point is already upstream of the plotted area, hence, this upstream retreat of the plunging is not evident in Fig. 8c. River mixing increased (Table 2) in response to E-winds. Total mixing was almost three times larger when the river was subject to E-winds of 6 m s^{-1} (run SW2) compared to conditions without any wind. Since the retreat of the plunge point upstream was only approximately 20 m, the increasing mixing rate was mainly the result of the increasing level of turbulence existing in the water column. Note, for example, in Table 2 that shear production at the confluence on day 203, under strong density differences, was six times larger when subject to moderate-to-strong E-winds (run SW2) compared with the conditions under no wind forcing.

The westerly winds, in turn, tended to accelerate the inflow along the main river, with an effect similar to increasing the Fr_{ic} and decreasing R_u in relation to the reference conditions, hence, displacing the plunge point downstream. On day 203, for example, with strong density differences, the plunge point moved in response to the W-winds from a position upstream of the junction apex into the confluence (Figs. 8e). With the plunging interface at the confluence, where horizontal shear at the interface from the side-stream flow increases, mixing rates tended to increase. Total mixing, in this case, was approximately 30% larger when compared with the reference conditions under no wind (see run SW5 in Table 2). The effects of W-winds on river mixing with moderate density contrasts between the rivers as observed on day 329 appeared contradictory. Total mixing under moderate density contrast decreased 15% (run SW15) in spite of increasing vertical shear (Table 2). But note that the tributary was forced to remain attached to its bank and the interface between the two rivers moved towards a more vertical position (Fig. 8j). The two rivers were forced by the winds to flow side by side within the study reach and the areas available for mixing decreased as the wind speed increased (see Fig. 8j) and, as a result, mixing decreased (runs SW15 and SW20 in

Table 2). The confinement of the tributary waters towards its bank under the influence of the strong westerly winds in Figs. 8j is similar to observations and simulations of river plumes under the influence of strong downwelling winds pushing the plume towards the coast (e.g., García Berdeal et al., 2002; Hickey et al., 1998; Otero et al., 2008). Fong and Geyer (2001) attributed the lower mixing rates observed in river plumes being confined under the influence of downwelling winds to a decrease in the contact area between the water from the river plume and the surrounding ambient water.

Winds acting along the tributary (S- and N-winds) control the intensity of the secondary circulation and, hence, the spatial distribution of the rivers at the confluence. Southerly winds, in general, weaken the secondary circulation that develops at the confluence because of the tributary inertia and its positive buoyancy. Depending on the wind speed and the density contrast, the tributary may even remain attached to its bank, along the left margin of the main channel. Note, for example, that on day 203, with strong density differences, the interface remained nearly horizontal independently of the wind forcing (Fig. 8d). On day 329, in turn, with moderate density contrasts, the tilting of the interface changed drastically in response to winds (see Fig. 8i). Under no wind forcing (Fig. 9c), and consistent with field observations (Figs. 9a,b), the secondary circulation within the confluence on day 329 became rapidly dominated by the tributary cell, that occupied all the channel cross-section and pushed water towards the right bank near the surface and towards the left bank near the bottom. As a result, under no wind forcing, the interface in the main channel was near the surface along the left margin (Fig. 8f). The S-winds counteract the inertia of the tributary and the baroclinic forces related to the density differences, reinforcing the W-cell (Fig. 9f). Under steady 6 m s^{-1} southerly winds, the two rivers were forced to flow side-by-side with a more vertical interface (Figs. 8i and 9f). The contact area available for mixing was in this case smaller than under the reference conditions, and hence, river mixing was weaker (Figs. 8i and Table 2). This is, for example, the case of run SW14 in Table 2, for which *TM* is approximately 27% weaker than *TM* under the reference conditions. In contrast to S-winds, N-winds tend to intensify the tributary cell (Fig 9d), favoring the upwelling of the W-river near the left bank (see Figs. 8b,g as an example) downstream of the confluence. This upwelling would displace the W-water and the mixing interface towards locations near the surface where wind shear is the largest, favoring river mixing. *TM* increases and the plunge point moves downstream in response to N-winds (see Figs. 8b,g, Table 2). These effects are consistent with an increase in R_u (Fig. 4). Easterly and westerly winds also changed the secondary circulation at the confluence on day 329. By decelerating the flow along the main river, easterly winds reinforce the tributary cell, which increases in strength (Fig. 9e) and mixing increases (runs SW12 and SW17). In contrast, by accelerating the flow along the main river, westerly winds reinforce the W-cell (Fig. 9g), which promotes the confinement of the N-river towards its bank (e.g., Fig. 8j) and a decrease in river mixing (runs SW15 and SW20 in Table 2).

Overall, it is possible to extract the following conclusion: for combinations of R_u and Fr_{ic} that result in locations of the plunge point upstream of the junction apex, wind forcing generally results in an increase in river mixing mainly due to an increase in velocity shear (Table 2). This is the case of the particular confluence analyzed here, where the strongest winds (commonly from the SE, Fig. 1h) tend to coincide with periods with strong buoyancy differences (Ramón et al., 2013). For combinations of R_u and Fr_{ic} that result in locations of plunge points downstream of the junction apex, in turn, winds could force (depending on wind direction) the two rivers to flow side by side for longer distances, decreasing the area available for mixing and ultimately decreasing mixing rates.

4.4 *Flow unsteadiness and plunging*

As instant values on Fig. 4 show, there is a high variability in time of both R_u and Fr_{ic} on the three simulated days (U-runs) due to the highly variable W-inflows (Figs. 1b-c). On day 203 all the combinations of R_u and Fr_{ic} lie above the isoline $x_{c\text{-}PL}$ = 0.93 in Fig. 4, which suggest that the plunge line was always located upstream of the confluence midpoint. Results of run U1 show that the plunge line between the W- and N-rivers was at all times located upstream of the confluence on day 203 (Fig. 10a), even at times of maximum W-discharges (Fig. 1b). This is consistent with the field observations on that day (Ramón et al., 2013). The magnitude of the inflows from the W-River (inertial forces) controlled how far upstream the plunge line moved within the W-channel, which was, at times, located immediately downstream of Mequinenza dam ($x_c \approx -6$) (Fig. 10a). On days 329 and 330, however, values in Fig. 4 lie upstream of, within, and downstream of the confluence. At the time when field data were collected (11-14 hr) and consistent with field observations (Ramón et al., 2013), the plunge point is located downstream of the confluence on day 329 (Figs. 10b), but it is located in the upstream mid half of the confluence or upstream of it on day 330 (see the location of the plunge point at time 35-38 hr in Figs. 10b). The plunge point also moved, however, to locations upstream of the confluence midpoint on day 329 during the time of zero withdrawals from Mequinenza and after the time of peak R_q (R_q = 0.58 at 16 hr, Fig. 1c) in the afternoon (Fig. 10b). The opposite occurred on day 330, when the plunge point moved to locations downstream of the confluence (Fig. 10b) after peak flows from the W-River in the evening (R_q = 0.13 at 20 hr in Fig. 1c).

In what follows, we will use the confluence midpoint (isoline $x_{c\text{-}PL}$ = 0.93 in Fig. 4) as a reference to understand the response of the plunge point to changes in R_u and

Fr_{ic} through time. As shown by the horizontal dark-gray shaded areas in Fig. 10b, there are times on days 329 and 330 in which the confluence exhibited the opposite to the expected pattern according to the steady inertia-buoyancy equilibrium (Fig. 4): that is, the plunge point is located downstream of $x_{c\text{-}PL} = 0.93$ when it was expected to be upstream of it (according to the instant values of R_u and Fr_{ic} at that time) or *vice versa*. For example, between 7.75-8.75 hr on day 329 (time interval B in Fig. 10b) values of R_u *vs*. Fr_{ic} lie below the isoline $x_{c\text{-}PL} = 0.93$ in Fig. 4, which would be indicative of the plunge point being located downstream of the confluence midpoint. During that time, however, the plunge point started moving from upstream locations towards downstream locations (Fig. 10b). This indicates the system needs time to adjust from one state to another, that is, the system needs time for the plunge point to move in the streamwise direction towards the new equilibrium position. Fig. 10c shows the time-varying W-inflow velocities on days 329 and 330 and the time-averaged velocity of the plunge-point displacement (u_{PL}) at the times when the location of the plunge point exhibited the reversed pattern. At times when the plunge point is moving from upstream to downstream locations (time intervals B, C, E and F in Fig. 10b), u_{PL} matches the advective velocity of the main stream u_W (Fig. 10c). At times when the plunge point is moving from downstream to upstream locations (time intervals A and D in Fig. 10b) u_{PL} becomes negative and could be as high as approximately -0.55 m s^{-1} (see time interval A in Fig. 10c). These high upstream velocities, however, do not reflect a real upstream movement of the plunge point because flow downstream of the confluence is mostly directed downstream, but are the result of the baroclinic time needed for the new N-water entering the confluence to reach the opposite margin. This time will depend on the lateral location of the mixing interface between rivers at the time the equilibrium R_u-Fr_{ic} changes towards a plunge point that should be located upstream of $x_{c\text{-}PL} = 0.93$. A and D time intervals in Fig. 10b cover 1 hr and 1.25 hr, respectively. The ≥ 1 hr time intervals approximate the baroclinic adjustment time $T_b = b_c/(g'\mathrm{D})^{0.5}$ of the confluence ($b_c \approx 380$ m being the average width of the confluence, Fig. 1a), which for days 329 and 330 are $T_{b\text{-}329} = 1.1$ hr, $T_{b\text{-}330} = 1.3$ hr.

4.5 Flow unsteadiness and mixing rates

Figs. 11a-c show the boxplots over time of the standard deviation σ of tracer concentration on days 203, 329 and 330 (U-runs in Table 1). On day 203 (Fig. 11a), σ is highly variable upstream of the confluence ($x_c < 0$), with σ changing from 0 to 20 ppm even immediately downstream of the Mequinenza dam ($x_c \approx -6$). σ values are on average > 0 ppm at $x_c \approx -6$ ($\sigma = \approx 5$ ppm, Fig. 11a), which indicates that on average some fraction of the N-water is able to reach locations immediately downstream of the Mequinenza dam. This high variability in σ upstream of the confluence is the result of the unsteadiness in the location of the plunge point between the W- and N- rivers (Fig. 10a). This variability, however, is damped downstream of the confluence ($x_c \geq 1.76$), with σ varying over time in a range of only 5 ppm at $x_c = 5.7$ (Fig. 11a). This low variability in σ is the result of the plunge point being always located upstream of the confluence (Fig. 10a), which allows the formation of a stable vertical stratification downstream of the confluence. The 24h-averaged σ results show average mixing rates of O (10^{-2}) ppm m^{-1} ($TM \approx 65\%$) (Table 2). This is one order of magnitude higher than mixing rates in the S1 run (steady-state in the absence of wind) and of the same order as mixing rates in the steady-state SW3 run (Table 2) in the presence of winds coming from the SE (as on day 203, Figs. 1d-f) with $U_{10} = 6$ m s^{-1}. This indicates that river mixing was primarily increased by the southeasterly winds blowing on that day and highlights the importance of the southeasterly winds in increasing river mixing during the stratification period in Ribarroja.

There is also variability in σ upstream of the confluence on days 329 and 330 (Figs. 11b-c). Time variability in σ is, however, restricted to a narrower area on those days, indicative of less capability of the N-water to flow upstream on top of the W-water in the W-channel. Note that the plunge point on both days is always located downstream of $x_c = -2$ (Fig. 10b) and that σ equals 0 ppm at $x_c < -3$ (Figs. 11b-c), which is indicative of pure (unmixed) W-water. Boxplots in Fig. 11b-c show that mixing downstream of the confluence is highly variable on both days 329 and 330, with σ values varying from 4 to 21 ppm and from 8 to 21 ppm at $x_c = 5.7$ on each day, respectively. This high variability in σ both upstream and downstream of the confluence is the result of the plunge point moving both upstream and downstream of the confluence on those days (Fig. 10b).

5. Summary and Conclusions

The confluence between the Ebro and Segre rivers has been presented as an example of a strongly-asymmetrical (junction angle of approximately 90º) large river confluence subject to strong density contrasts between the confluent rivers. The location of the plunge point between the rivers, at this confluence, is controlled by an inertia-buoyancy equilibrium that can be expressed in terms of the velocity ratio and a confluence Froude number. The plunge point between rivers will move to upstream locations as the confluence Froude number decreases and/or the velocity ratio increases (for low velocity ratios). As the velocity ratio (tributary inertia) keeps increasing, though, the plunge point tends to move to downstream locations due to the increasing rates of turbulent diffusion that tend to keep the tributary flow attached to bed, shifting the orientation of the mixing interface towards more vertical positions.

River mixing downstream of the confluence is strongly dependent on the location of the plunge point between the confluent rivers. The largest mixing rates occur when the plunge point is located at the confluence itself due to a combination of an enhanced contact area along the interface between the rivers and of high mixing coefficients, especially in the vertical direction. As the plunge point moves upstream of the junction apex, mixing rates decrease as a result of a decrease in the magnitude of vertical eddy diffusivities within a horizontal mixing interface. Mixing rates also decrease as the plunge point moves to locations downstream of the confluence as a result of a decrease in the total area of contact between the confluent rivers.

The effect of wind forcing on the spatial arrangement of the confluent rivers depends on both wind velocity and direction, but can completely alter the inertia-buoyancy equilibrium at the confluence and even move the location of the plunge point from locations upstream of the junction apex to locations downstream of the confluence, and hence, modify river mixing rates. Winds opposite to the direction of the main stream are more effective in increasing shear at the confluence, and in turn, in increasing river mixing.

Unsteady river-inflows change the streamwise equilibrium location of the plunge point through time, which means that for a given density contrast the plunge point can move from locations upstream of the confluence to locations downstream of the confluence, and *vice versa,* due to changes in river inflows alone. This is important because mixing rates decrease as the plunge point moves to locations upstream of the confluence. There is a delay in time between the shift in the equilibrium conditions and the corresponding streamwise movement of the plunge point.

Although buoyancy and wind effects are shown to be important in this confluence, the characteristics of this confluence are transitional between a lake and a river, which poses limitations on the general applicability of these findings to all river confluences.

Acknowledgements

This work was part of a collaborative agreement between the University of Barcelona and the University of Granada to work jointly in the Project '*Gestión hidráulica y técnicas de detección remota aplicada al control de poblaciones mejillón cebra: el caso del embalse de Ribarroja y el tramo inferior del río Ebro*', funded by the Spanish Ministry of the Environment. The parallel version of the hydrodynamic model was developed under project CGL2008-06101/BOS, funded by the Spanish Ministry of Science and Innovation. The first author was supported by a PhD grant (*Programa Estatal de Promoción del Talento y su Empleabiliad: Subprograma de Formación de Profesorado Universitario*) from the Spanish Government. We thank Joan Armengol, Josep Dolz and the Flumen Institute for making its data available for us. We are indebted to Toni Palau and the scientific personnel from ENDESA-Medio Ambiente. We are grateful for the insightful comments of Ben Hodges and Bruce Rhoads during the review process.

Notation

The following symbols are used in this paper:

b_p = post-confluence channel-width, m

b_c = average width of the confluence, m

C = tracer concentration, ppm

C_d = bottom drag coefficient

C_p = theoretical concentration after complete mixing, ppm

D = depth, m

d = layer depth, m

Fr_i = internal Froude number

g = acceleration due to gravity, m s^{-2}

g' = reduced gravity (= $g\ \Delta\rho/\rho_0$), m s^{-2}

K_h = horizontal eddy diffusivity, m^2 s^{-1}

K_z = vertical eddy diffusivity, m^2 s^{-1}

L_z = distance downstream where full vertical mixing is achieved in a two-layered system, m

P_s = shear production of TKE, m^2 s^{-3}

P_{sk} = stirring (TKE), m^2 s^{-3}

Q = discharge, m^3 s^{-1}

R_m = momentum flux ratio (= $[u_N\ Q_N\ \rho_N] / [u_W\ Q_W\ \rho_W]$)

R_q = discharge ratio (= Q_N/Q_W)

R_s = radius of curvature, m

$R_{sk\text{-}s}$ = stirring-to-shear ratio.

$R_{sk\text{-}sk0}$= stirring-to-stirring ratio.

$R_{s\text{-}s0}$ = shear-to-shear ratio.

R_u = velocity ratio (= u_N/u_W)

S_h = area available for horizontal mixing, m^2

S_z = area available for vertical mixing, m^2

s = distance downstream of the junction apex, m

TM = total mixing, %

T_b = baroclinic adjustment time, s

U_{10} = wind velocity at 10 m height, m s^{-1}

u = inflow velocity, m s^{-1}

$u*$ = friction velocity, m s^{-1}

$u_{n\text{-}rsm}$ = root mean square secondary velocity, m s^{-1}

u_s = streamwise velocity, m s^{-1}

u_{PL} = velocity of the plunge-point displacement, m s^{-1}

V = Volume, m^3

x_c = non-dimensional distance downstream of the junction apex

$x_{c\text{-}PL}$ = non-dimensional streamwise location of the plunge point

Δt = time step of the simulations, s

Δx, Δy, Δz = grid cell sizes in the x-, y- and z- direction, m

δ = ratio of the scales for the vertical and horizontal variability of the flow.

ε_t = transverse mixing coefficient, m^2 s^{-1}

ρ = water density, kg m^{-3}

ρ_0 = reference density (= 1000 kg m^{-3})

$\Delta\rho$ = density difference between rivers, kg m^{-3}

σ = standard deviation of tracer concentrations, ppm

σ_0 = standard deviation of tracer concentrations if no mixing occurs, ppm

$\Delta\sigma/s$ = mixing rates, ppm m^{-1}

Φ = wind direction, º

Subscripts

W = Ebro River

N = Segre River

c = confluence

0 = reference value

Appendix A. Supplementary material

References

Acosta, M., Anguita, M., Rueda, F.J., Fernández-Valdomero, F., 2010. Parallel implementation of a semi-implicit 3D lake hydrodynamic model, in: Proceedings of the International Conference on Computational and Mathematical Methods in Science and Engineering, Add/link/COMSOL. Almería, Spain, pp. 1026–1037.

Arneborg, L., Fiekas, V., Umlauf, L., Burchard, H., 2007. Gravity Current Dynamics and Entrainment—A Process Study Based on Observations in the Arkona Basin. J. Phys. Oceanogr. 37, 2094–2113. doi:10.1175/JPO3110.1

Ashmore, P.E., Ferguson, R.I., Prestegaard, K.L., Ashworth, P.J., Paola, C., 1992. Secondary Flow in Anabranch Confluences of a Braided, Gravel-Bed Stream. Earth Surf. Process. Landforms 17, 299–311. doi:10.1002/esp.3290170308

Benda, L., Poff, N.L., Miller, D., Dunne, T., Reeves, G., Pess, G., Pollock, M., 2004. The Network Dynamics Hypothesis: How Channel Networks Structure Riverine Habitats. Bioscience 54, 413–427. doi:10.1641/0006-3568(2004)054[0413:TNDHHC]2.0.CO;2

Bigelow, P.E., Benda, L.E., Miller, D.J., Burnett, K.M., 2007. On debris flows, river networks, and the spatial structure of channel morphology. For. Sci. 53, 220–238. doi:10.1016/j.neuroimage.2011.08.082

Biron, P., De Serres, B., Roy, A.G., Best, J.L., 1993. Shear layer turbulence at an unequal depth channel confluence, in: Clifford, N.J., French, J.R., Hardisty, J. (Eds.), Turbulence: Perspectives on Flow and Sediment Transport. John Wiley & Sons, Chichester, pp. 197–213.

Biron, P., Ramamurthy, A., Han, S., 2004. Three-Dimensional Numerical Modeling of Mixing at River Confluences. J. Hydraul. Eng. 130, 243–253. doi:10.1061/(ASCE)0733-9429(2004)130:3(243)

Bournet, P., Dartus, D., Tassin, B., Vinçon-Leite, B., 1999. Numerical Investigation of Plunging Density Current. J. Hydraul. Eng. 125, 584–594. doi:10.1061/(ASCE)0733-9429(1999)125:6(584)

Bradbrook, K.F., Lane, S.N., Richards, K.S., 2000. Numerical simulation of three-dimensional, time-averaged flow structure at river channel confluences. Water Resour. Res. 36, 2731–2746. doi:10.1029/2000WR900011

Chu, V., Babarutsi, S., 1988. Confinement and Bed Friction Effects in Shallow Turbulent Mixing Layers. J. Hydraul. Eng. 114, 1257–1274. doi:10.1061/(ASCE)0733-9429(1988)114:10(1257)

Chua, V.P., Fringer, O.B., 2011. Sensitivity Analysis of Three-Dimensional Salinity Simulations in North San Francisco Bay Using the Unstructured-Grid SUNTANS Model. Ocean Model. 39, 332–350. doi:http://dx.doi.org/10.1016/j.ocemod.2011.05.007

Chung, S., Gu, R., 1998. Two-Dimensional Simulations of Contaminant Currents in Stratified Reservoir. J. Hydraul. Eng. 124, 704–711. doi:10.1061/(ASCE)0733-9429(1998)124:7(704)

Constantinescu, G., Miyawaki, S., Rhoads, B., Sukhodolov, A., 2012. Numerical analysis of the effect of momentum ratio on the dynamics and sediment-entrainment capacity of coherent flow structures at a stream confluence. J. Geophys. Res. 117, F04028. doi:10.1029/2012JF002452

Constantinescu, G., Miyawaki, S., Rhoads, B., Sukhodolov, A., Kirkil, G., 2011. Structure of turbulent flow at a river confluence with momentum and velocity ratios close to 1: Insight provided by an eddy-resolving numerical simulation. Water Resour. Res. 47, W05507. doi:10.1029/2010WR010018

Cook, C.B., Richmond, M.C., Titzler, S.P., Dibrani, B., Bleich, M.D., Fu, T., 2006. Hydraulic Characteristics of the Lower Snake River During Periods of Juvenile

Fall Chinook Salmon Migration. Report PNNL-15532. Pacific North West National Laboratory. Prepared for the Bonneville Power Administration, U.S. Department of Energy.Richland, Washington. pp. 176.

Cortés, A., Rueda, F.J., Wells, M.G., 2014. Experimental Observations of the Splitting of a Gravity Current at a Density Step in a Stratified Water Body. J. Geophys. Res. Ocean. 119, 1038–1053. doi:10.1002/2013JC009304

Cruzado, A., Velásquez, Z., Pérez, M. del C., Bahamón, N., Grimaldo, N.S., Ridolfi, F., 2002. Nutrient fluxes from the Ebro River and subsequent across-shelf dispersion. Cont. Shelf Res. 22, 349–360. doi:http://dx.doi.org/10.1016/S0278-4343(01)00060-7

Dallimore, C., Imberger, J., Ishikawa, T., 2001. Entrainment and Turbulence in Saline Underflow in Lake Ogawara. J. Hydraul. Eng. 127, 937–948. doi:10.1061/(ASCE)0733-9429(2001)127:11(937)

Durran, D.R., 1999. Numerical Methods for Wave Equations in Geophysical Fluid Dynamics, 1st Editio. ed. Springer-Verlag, New York.

Fischer, H.B., List, E.J., Koh, R.C.Y., Imberger, J., Brooks, N.H., 1979. Mixing in Inland and Coastal Waters. Academic Press, New York.

Fischer, H.B., Smith, R.D., 1983. Observations of Transport to Surface Waters from a Plunging Inflow to Lake Mead. Limnol. Oceanogr. 28, 258–272.

Fong, D.A., Geyer, W.R., 2001. Response of a River Plume During an Upwelling Favorable Wind Event. J. Geophys. Res. Ocean. 106, 1067–1084. doi:10.1029/2000JC900134

García Berdeal, I., Hickey, B.M., Kawase, M., 2002. Influence of wind stress and ambient flow on a high discharge river plume. J. Geophys. Res. Ocean. 107, 13–24. doi:10.1029/2001JC000932

Gaudet, J.M., Roy, A.G., 1995. Effect of Bed Morphology on Glow Mixing Length at River Confluences. Nature 373, 138–139.

Gleichauf, K.T., Wolfram, P.J., Monsen, N.E., Fringer, O.B., Monismith, S.G., 2014. Dispersion Mechanisms of a Tidal River Junction in the Sacramento–San Joaquin Delta, California. San Fr. Estuary Watershed Sci. 12 (4).

Gooseff, M.N., Bencala, K.E., Wondzell, S.M., 2008. Solute transport along stream and river networks, in: Rice, S.P., Roy, A.G., Rhoads, B.L. (Eds.), River Confluences, Tributaries and the Fluvial Network. John Wiley & Sons, Chichester, pp. 395–418.

Gross, E., Koseff, J., Monismith, S., 1999. Three-Dimensional Salinity Simulations of South San Francisco Bay. J. Hydraul. Eng. 125, 1199–1209. doi:10.1061/(ASCE)0733-9429(1999)125:11(1199)

Hickey, B.M., Pietrafesa, L.J., Jay, D.A., Boicourt, W.C., 1998. The Columbia River Plume Study: Subtidal variability in the velocity and salinity fields. J. Geophys. Res. Ocean. 103, 10339–10368. doi:10.1029/97JC03290

Kantha, L.H., Clayson, C.A., 1994. An improved mixed layer model for geophysical applications. J. Geophys. Res. Ocean. 99, 25235–25266. doi:10.1029/94JC02257

Kassem, A., Imran, J., Khan, J., 2003. Three-Dimensional Modeling of Negatively Buoyant Flow in Diverging Channels. J. Hydraul. Eng. 129, 936–947. doi:10.1061/(ASCE)0733-9429(2003)129:12(936)

Kiffney, P.M., Greene, C.M., Hall, J.E., Davies, J.R., 2006. Tributary streams create spatial discontinuities in habitat, biological productivity, and diversity in mainstem rivers. Can. J. Fish. Aquat. Sci. 63, 2518–2530. doi:10.1139/f06-138

Konsoer, K., Rhoads, B., 2014. Spatial–Temporal Structure of Mixing Interface Turbulence at Two Large River Confluences. Environ. Fluid Mech. 14, 1043–1070. doi:10.1007/s10652-013-9304-5

Lane, S.N., Parsons, D.R., Best, J.L., Orfeo, O., Kostaschuk, R.A., Hardy, R.J., 2008. Causes of Rapid Mixing at a Junction of Two Large Rivers: Río Paraná and Río Paraguay, Argentina. J. Geophys. Res. Earth Surf. 113, F02024. doi:10.1029/2006JF000745

Lewis, Q.W., Rhoads, B.L., 2015. Rates and Patterns of Thermal Mixing at a Small Stream Confluence Under Variable Incoming Flow Conditions. Hydrol. Process. 29, 4442–4456. doi:10.1002/hyp.10496

Llebot, C., Rueda, F.J., Solé, J., Artigas, M.L., Estrada, M., 2014. Hydrodynamic States in a Wind-Driven Microtidal Estuary (Alfacs Bay). J. Sea Res. 85, 263–276. doi:http://dx.doi.org/10.1016/j.seares.2013.05.010

Lung, W., O’Connor, D., 1984. Two Dimensional Mass Transport in Estuaries. J. Hydraul. Eng. 110, 1340–1357. doi:10.1061/(ASCE)0733-9429(1984)110:10(1340)

Lyubimova, T., Lepikhin, A., Konovalov, V., Parshakova, Y., Tiunov, A., 2014. Formation of the Density Currents in the Zone of Confluence of Two Rivers. J. Hydrol. 508, 328–342. doi:http://dx.doi.org/10.1016/j.jhydrol.2013.10.041

Mellor, G.L., Yamada, T., 1974. A Hierarchy of Turbulence Closure Models for Planetary Boundary Layers. J. Atmos. Sci. 31, 1791–1806. doi:10.1175/1520-0469(1974)031<1791:AHOTCM>2.0.CO;2

Morillo, S., Imberger, J., Antenucci, J., Woods, P., 2008. Influence of Wind and Lake Morphometry on the Interaction between Two Rivers Entering a Stratified Lake. J. Hydraul. Eng. 134, 1579–1589. doi:10.1061/(ASCE)0733-9429(2008)134:11(1579)

Otero, P., Ruiz-Villarreal, M., Peliz, A., 2008. Variability of River Plumes off Northwest Iberia in Response to Wind Events. J. Mar. Syst. 72, 238–255. doi:http://dx.doi.org/10.1016/j.jmarsys.2007.05.016

Parsons, D.R., Jackson, P.R., Czuba, J.A., Engel, F.L., Rhoads, B.L., Oberg, K.A., Best, J.L., Mueller, D.S., Johnson, K.K., Riley, J.D., 2013. Velocity Mapping Toolbox (VMT): a processing and visualization suite for moving-vessel ADCP measurements. Earth Surf. Process. Landforms 38, 1244–1260. doi:10.1002/esp.3367

Prats, J., 2011. El Règim Tèrmic del Tram Inferior de l'Ebre i les seues Alteracions. Ph.D. thesis, Escola Te`cnica Superior d'Enginyers de Camins, Canals i Ports de Barcelona, Inst. Flumen,Tech. Univ. Catalonia.

Prats, J., Arbat-Bofill, M., Martí-Cardona, B., Dolz, J., Armengol, J., 2013. Utilidad de los Sensores Térmicos Aerotransportados en Estudios de Hidrodinámica de Embalses y Ríos, in: III Jornadas de Ingeniería Del Agua. Valencia, Spain.

Prats, J., Armengol, J., Marcé, R., Sánchez-Juny, M., Dolz, J., 2010. Dams and Reservoirs in the Lower Ebro River and Its Effects on the River Thermal Cycle, in: Barceló, D., Petrovic, M. (Eds.), The Ebro River Basin SE - 68, The Handbook of Environmental Chemistry. Springer Berlin Heidelberg, pp. 77–95. doi:10.1007/698_2010_68

Ramón, C.L., Armengol, J., Dolz, J., Prats, J., Rueda, F.J., 2014. Mixing Dynamics at the Confluence of Two Large Rivers Undergoing Weak Density Variations. J. Geophys. Res. Ocean. 119, 2386–2402. doi:10.1002/2013JC009488

Ramón, C.L., Hoyer, A.B., Armengol, J., Dolz, J., Rueda, F.J., 2013. Mixing and circulation at the confluence of two rivers entering a meandering reservoir. Water Resour. Res. 49, 1429–1445. doi:10.1002/wrcr.20131

Ramón, C.L., Prats, J., Rueda, F.J., 2015. Simulation of Turbulent Flows in River Confluences and Meandering Channels with a Cartesian 3D Free Surface Hydrodynamic Model. Int. J. Comput. Methods 1550035. doi:10.1142/S0219876215500358

Rhoads, B.L., Kenworthy, S.T., 1998. Time-Averaged Flow Structure in the Central Region of a Stream Confluence. Earth Surf. Process. Landforms 23, 171–191. doi:10.1002/(SICI)1096-9837(199802)23:2<171::AID-ESP842>3.0.CO;2-T

Rhoads, B.L., Kenworthy, S.T., 1995. Flow Structure at an Asymmetrical Stream Confluence. Geomorphology 11, 273–293. doi:http://dx.doi.org/10.1016/0169-555X(94)00069-4

Rhoads, B.L., Sukhodolov, A.N., 2001. Field Investigation of Three-Dimensional Flow Structure at Stream Confluences: 1. Thermal Mixing and Time-Averaged Velocities. Water Resour. Res. 37, 2393–2410. doi:10.1029/2001WR000316

Rice, S.P., Ferguson, R.I., Hoey, T.B., 2006. Tributary Control of Physical Heterogeneity and Biological Diversity at River Confluences. Can. J. Fish. Aquat. Sci. 63, 2553–2566. doi:10.1139/f06-145

Rodi, W., 2010. Large eddy simulation of river flows, in: Proceedings of the Int. Conf.

Fluvial Hydraulics (River Flow). Graunschweig, Germany, pp. 23–32.

Roe, P.L., 1984. Generalized formulation of TVD Lax-Wendroff schemes. ICASE Rep, 84–53, NASA CR-172478, NASA Langley Res. Cent. Hampton, VA, USA.

Rozovskii, I.L., 1961. Flow of Water in Bends of Open Channels: Israel Program for Scientific Translation. OTS 60-51133, US Department of Commerce, Washington, DC (Originally published by Acad. of Sci. of the Ukrainian SSR, 1957, pp. 233).

Rueda, F.J., MacIntyre, S., 2010. Modelling the Fate and Transport of Negatively Buoyant Storm–River Water in Small Multi-Basin Lakes. Environ. Model. Softw. 25, 146–157. doi:http://dx.doi.org/10.1016/j.envsoft.2009.07.002

Rutherford, V.J.C., 1994. River mixing. John Wiley & Sons, Chichester.

Smith, P., 2006. A Semi-Implicit, Three-Dimensional Model of Estuarine Circulation. Open File Report 2006-1004, USGS, Sacramento, USA.

Uijttewaal, W.S.J., Booij, R., 2000. Effects of Shallowness on the Development of Free-Surface Mixing Layers. Phys. Fluids 12.

van Leer, B., 1974. Towards the Ultimate Conservative Difference Scheme. II. Monotonicity and Conservation Combined in a Second-Order Scheme. J. Comput. Phys. 14, 361–370. doi:http://dx.doi.org/10.1016/0021-9991(74)90019-9

Wang, B., Fringer, O.B., Giddings, S.N., Fong, D.A., 2009. High-Resolution Simulations of a Macrotidal Estuary Using SUNTANS. Ocean Model. 28, 167–192. doi:http://dx.doi.org/10.1016/j.ocemod.2008.08.008

Wang, B., Giddings, S.N., Fringer, O.B., Gross, E.S., Fong, D.A., Monismith, S.G., 2011. Modeling and Understanding Turbulent Mixing in a Macrotidal Salt Wedge Estuary. J. Geophys. Res. Ocean. 116. doi:10.1029/2010JC006135

Wells, M., Nadarajah, P., 2009. The Intrusion Depth of Density Currents Flowing into Stratified Water Bodies. J. Phys. Oceanogr. 39, 1935–1947. doi:10.1175/2009JPO4022.1

Wolfram, P.J., Fringer, O.B., Monsen, N.E., Gleichauf, K.T., Fong, D.A., Monismith, S.G., 2016. Modeling Intrajunction Dispersion at a Well-Mixed Tidal River Junction. J. Hydraul. Eng. In press. doi:10.1061/(ASCE)HY.1943- 7900.0001108

Table 1. Model inputs for the simulation runs

Run case	**JD**[a]	$\Delta\rho/\rho_0$	Q_W **(m^3/s)**	Q_N **(m^3/s)**	R_u	R_q	R_m	Fr_{ic}	U_{10} **(m/s)**	Φ[b] **(°)**
A-series	-	1.01×10^{-4}, 1.4×10^{-3} or 4.7×10^{-3}	34 to 351	6 to 944	0.15 to 18	0.1 to 11.8	0.015 to 213	0.04 to 2	0	-
Runs with steady flows:										
S1	203	1.4×10^{-3}	86	57	1.02	0.58	0.67	0.13	0	-
S2	329	1.01×10^{-4}	138	51	0.57	0.37	0.21	0.79	0	-
S3	330	7×10^{-5}	61	43.5	1.09	0.71	0.78	0.42	0	-
Runs with steady flows and constant wind forcing:										
SW1	203	1.4×10^{-3}	86	57	1.02	0.58	0.67	0.13	6	0
SW2	203	1.4×10^{-3}	86	57	1.02	0.58	0.67	0.13	6	90
SW3	203	1.4×10^{-3}	86	57	1.02	0.58	0.67	0.13	6	135
SW4	203	1.4×10^{-3}	86	57	1.02	0.58	0.67	0.13	6	180
SW5	203	1.4×10^{-3}	86	57	1.02	0.58	0.67	0.13	6	270
SW6	203	1.4×10^{-3}	86	57	1.02	0.58	0.67	0.13	12	0
SW7	203	1.4×10^{-3}	86	57	1.02	0.58	0.67	0.13	12	90
SW8	203	1.4×10^{-3}	86	57	1.02	0.58	0.67	0.13	12	135
SW9	203	1.4×10^{-3}	86	57	1.02	0.58	0.67	0.13	12	180
SW10	203	1.4×10^{-3}	86	57	1.02	0.58	0.67	0.13	12	270
SW11	329	1.01×10^{-4}	138	51	0.57	0.37	0.21	0.79	6	0
SW12	329	1.01×10^{-4}	138	51	0.57	0.37	0.21	0.79	6	90
SW13	329	1.01×10^{-4}	138	51	0.57	0.37	0.21	0.79	6	135
SW14	329	1.01×10^{-4}	138	51	0.57	0.37	0.21	0.79	6	180
SW15	329	1.01×10^{-4}	138	51	0.57	0.37	0.21	0.79	6	270
SW16	329	1.01×10^{-4}	138	51	0.57	0.37	0.21	0.79	12	0
SW17	329	1.01×10^{-4}	138	51	0.57	0.37	0.21	0.79	12	90
SW18	329	1.01×10^{-4}	138	51	0.57	0.37	0.21	0.79	12	135
SW19	329	1.01×10^{-4}	138	51	0.57	0.37	0.21	0.79	12	180
SW20	329	1.01×10^{-4}	138	51	0.57	0.37	0.21	0.79	12	270
Runs with unsteady flows and wind forcing (field conditions):										
U1	203	1.4×10^{-3}	0-288	57	f(t)[c]	f(t)	f(t)	f(t)	f(t)	f(t)
U2	329	1.01×10^{-4}	0-344	51	f(t)	f(t)	f(t)	f(t)	f(t)	f(t)
U3	330	7×10^{-5}	0-340	43.5	f(t)	f(t)	f(t)	f(t)	f(t)	f(t)

[a] JD = Julian day.

[b] 0° = northerly winds.

[b] f(t) = values are variable in time.

Table 2. Absolute values of the time-averaged mixing rates and total mixing at $x_c = 5.7$, location of the plunge point and ratios of time-averaged energy available through stirring and shear within the domain volume between $0 \le x_c \le 5.7$. The presence of hyphens indicates that term has not been evaluated in that simulation.

Run case	**Julian day**	**$\Delta\sigma/s$ (ppm m^{-1})**	***TM* (%)**	**$x_{c\text{-}PL}$**	**$R_{sk\text{-}s}$ [a,b] (%)**	**$R_{sk\text{-}sk0}$ [c]**	**$R_{s\text{-}s0}$ [d]**
S1	203	6.2×10^{-3}	29.0	−5.35	1	-	-
S2	329	1.2×10^{-2}	64.0	1.52	28	-	-
S3	330	1.4×10^{-2}	66.4	0.89	11	-	-
SW1	203	1.0×10^{-2}	46.8	−1.23	1	3.4	4.4
SW2	203	1.7×10^{-2}	80.9	−5.40	2	7.8	6.0
SW3	203	1.6×10^{-2}	72.0	−5.29	3	12.6	4.8
SW4	203	8.8×10^{-3}	41.1	−2.10	10	19.9	2.5
SW5	203	1.3×10^{-2}	61.8	1.27	14	71.5	6.3
SW6	203	2.0×10^{-2}	91.9	1.14	3	49.8	17.7
SW7	203	2.1×10^{-2}	99.2	−1.60	5	119.8	27.6
SW8	203	2.1×10^{-2}	95.6	−1.48	1	12.6	27.8
SW9	203	1.6×10^{-2}	71.9	−1.48	13	144.5	13.3
SW10	203	1.8×10^{-2}	82.1	5.64	7	130.6	21.7
SW11	329	1.6×10^{-2}	84.1	3.02	25	5.91	4.6
SW12	329	1.8×10^{-2}	93.1	1.15	15	4.81	6.3
SW13	329	1.9×10^{-2}	95.5	0.89	11	2.90	5.3
SW14	329	7.3×10^{-3}	37.3	>5.7	0	0.02	2.7
SW15	329	9.8×10^{-3}	50.5	>5.7	19	3.8	3.9
SW16	329	1.5×10^{-2}	78.2	5.27	12	12.3	20.0
SW17	329	1.9×10^{-2}	97.8	1.02	2	3.73	46.3
SW18	329	1.9×10^{-2}	95.9	1.40	6	15.2	49.6
SW19	329	1.7×10^{-2}	88.9	>5.7	4	3.6	18.6
SW20	329	7.7×10^{-3}	39.7	>5.7	7	7.0	20.4
U1	203	1.4×10^{-2}	65.5	-	-	-	-
U2	329	1.5×10^{-2}	79.1	-	-	-	-
U3	330	1.6×10^{-2}	72.8	-	-	-	-

[a] V = volume of the domain downstream of $x_c > 0$, ‹› = time-averaged values.

[b] $R_{sk\text{-}s} = \sum_V \langle \rho P_{sk} \rangle \Big/ \sum_V \langle \rho P_s \rangle \times 100$

[c] $R_{sk\text{-}sk0} = \sum_V \langle \rho P_{sk} \rangle \Big/ \sum_V \langle \rho P_{sk} \rangle_{U10=0}$, where the subscript "$U_{10}$=0" refers to the steady simulation without wind forcing (here S1 or S2)

[d] $R_{s\text{-}s0} = \sum_V \langle \rho P_s \rangle \Big/ \sum_V \langle \rho P_s \rangle_{U10=0}$

Figure 1. (a) Ribarroja reservoir, model domain (shaded gray area) and bathymetry of the region of interest (rectangle). The location is shown for the N-River inflow sections (N1 and N2), three of the W sections in the W-channel, three of the A-sections, one of the ADCP transect collected in the field on day 329 (transect F) at the confluence region, and three of the B sections downstream of the confluence. (b, c) Inflow rates from the W- and N- rivers, and hourly-averaged (d-e) wind velocities and (f, g) directions on (b, d, f) day 203 and (c, e, g) days 329-330 in 2009. (h) Wind rose for the whole year 2009 at the Ribarroja reservoir. The wind rose in (h) shows directions the wind was blowing towards.

Figure 2. Combinations of R_u and Fr_{ic} occurring at the confluence during the stratification period (summer and autumn), calculated from daily-averaged historical discharges, temperatures and conductivities collected at the confluence in 1998, 1999, 2003 and 2004 (for details on the density and flow data from which R_u and Fr_{ic} were calculated, see Prats (2011) and Prats et al. (2010)). Situations in which the W-River is denser (black dots) than the N-River account for 63% of the time. The shaded area shows the range of R_u and Fr_{ic} values analyzed in the A-series.

Figure 3. Expected shapes of standard deviations of tracer concentration in the streamwise direction if (a) the tributary is not able to flow upstream into the main river channel (σ = 0 ppm at distances < 0) and no mixing occurs between rivers downstream of the junction apex ($\sigma = \sigma_0$ at distances > 0), (b) the tributary is not able to flow upstream into the main river channel but river mixing occurs downstream of the junction apex and (c) some fraction of the tributary is able to flow upstream into the

main river channel until distance x_{up} and river mixing occurs downstream of the confluence.

Figure 4. Results of the A-series of simulations. Time-averaged linearly-interpolated total mixing *TM* (%) and time-averaged location of the plunge point $x_{c\text{-}PL}$ (white solid isolines) as function of R_u (left *y*-axis) and Fr_{ic}. Gray dots represent the actual values of R_u and Fr_{ic} tested (see Table 1). The dashed black line identifies the Fr_{ic} values for which the largest total mixing *TM* occurs for a given R_u. The location is also shown for the daily-averaged (black-encircled white dots) and instant R_u vs. Fr_{ic} observed on Julian days 203 (stars), 329 (black dots) and 330 (crosses). Black square shows the daily-averaged conditions observed by Prats et al. (2013). The horizontal and vertical black lines mark R_u values = 0.5 and Fr_{ic} values = 0.67, respectively. For a more complete description, the right *y*-axis show the corresponding values of R_m for a given value of R_u in the left *y*-axis.

Figure 5. (a-d) Time-averaged location of the mixing interface (magenta) between the W-(Ebro) and N-(Segre) rivers, area of the mixing interface available for (e) horizontal S_h and (f) vertical S_z mixing, (g) average value of K_z within the mixing interface, and (h) width-averaged $u_{n\text{-}rms}$ in section A5. Simulations in A-series with Fr_{ic} = 0.45 and (a) R_u = 0.15, (b) R_u = 0.4, (c) R_u = 2.5, and (d) R_u = 8.9. Black lines in (a-c) show the location of the plunge line. Gray shaded areas in (e-h) show simulations in which plunging occurs within the confluence. Values of S_h, S_z and K_z are evaluated for the whole extension of the mixing layer within the study reach ($-6 \leq x_c \leq 5.6$). The aspect ratio (*x*:*y*:*z*) in (a-d) is 40:20:1

Figure 6. Instant values of (a-c) tracer concentrations (ppm) and (d-f) vertical vorticities (s^{-1}) at the surface plane for simulations in A-series with Fr_{ic} = 0.45 and (a, d) R_u = 8.9, (b, e) R_u = 5.4 and (c, f) R_u = 2.5. Black isolines in (a-c) show tracer concentrations $C = C_p$. Black arrows in (c-d) show the location of eddies within the mixing layer.

Figure 7. (a-d) Time-averaged location of the mixing interface (magenta) between the W-(Ebro) and N-(Segre) rivers, area of the mixing interface available for (e) horizontal S_h and (f) vertical S_z mixing and average value of (g) K_z within the mixing interface for simulations in A-series with R_u = 1.2 and (a) Fr_{ic} = 0.12, (b) Fr_{ic} = 0.34, (c) Fr_{ic} = 0.80, and (d) Fr_{ic} = 1.5. Black lines in (a-d) show the location of the plunge line. Gray shaded areas in (e-g) show simulations in which plunging occurs within the confluence. Values of S_h, S_z and K_z are evaluated for the whole extension of the mixing layer within the study reach ($-6 \leq x_c \leq 5.6$). The aspect ratio (x:y:z) in (a-d) is 40:20:1

Figure 8. Time-averaged spatial arrangement of the Ebro (W-) water (red), the Segre (N-) water (blue), and the mixing interface (magenta) for constant wind velocities of 6 m s^{-1} and different directions. Runs (a) S1, (b) SW1, (c) SW2, (d) SW4, (e) SW5, (f) S2, (g) SW11, (h) SW12, (i) SW14 and (j) SW15 in Table 1. The y-axis is aligned with the North direction. The Ebro and Segre waters are 60% opaque. Aspect ratio (x:y:z) 40:20:1.

Figure 9. Secondary circulation at section F (see its location in Fig. 1a). (a) Instant secondary circulation measured with an ADCP in the field around 13 hr on day 329, (b) instant secondary circulation predicted by the model in the simulation of field conditions (run U2) at the time the ADCP transect was collected, and (c-g) time-averaged secondary circulation in (c) the simulation under steady-state in the absence of wind (run S2) and (d-g) the simulations under steady-state with a constant wind forcing of 6 m s^{-1} from the (d) North (run SW11), (e) East (run SW12), (f) South (run SW14) and (g) West (run SW15). Dark and light gray colors in c-g show the location of the W-River and the mixing layer, respectively. Secondary circulation was calculated with the Rozovskii method (Parsons et al., 2013; Rozovskii, 1961). Arrows show the main pattern of recirculation.

Figure 10. (a,b) Variation with time of the streamwise location of the plunge point (x_{c-PL}) between the W- and N- rivers on days (a) 203 (run U1) and (b) 329-330 (runs U2 and U3). And (c) variation with time of the W-inflow velocities (u_W) and average velocities of the streamwise displacement of the plunge line (u_{PL}) at times (A-F horizontal dark-gray shaded areas) when the location of the plunge line is opposite (upstream of or downstream of) to that expected according to the isoline x_{c-PL} =0.93 (see Fig. 4 and section 4.1 for further details) on days 339-330. Vertical light-gray shaded areas in (a, b) show the location of the confluence region and gray dotted lines in (a, b) show the location of the confluence midpoint.

Figure 11. Boxplots of standard deviations (σ) of tracer concentrations over a 24 hr period upstream, at, and downstream of the confluence on days (a) 203, (b) 329 and (c)

330. The shaded areas show the location of the Confluence region ($0 \leq x_c \leq 1.76$). U-runs in Table 1.

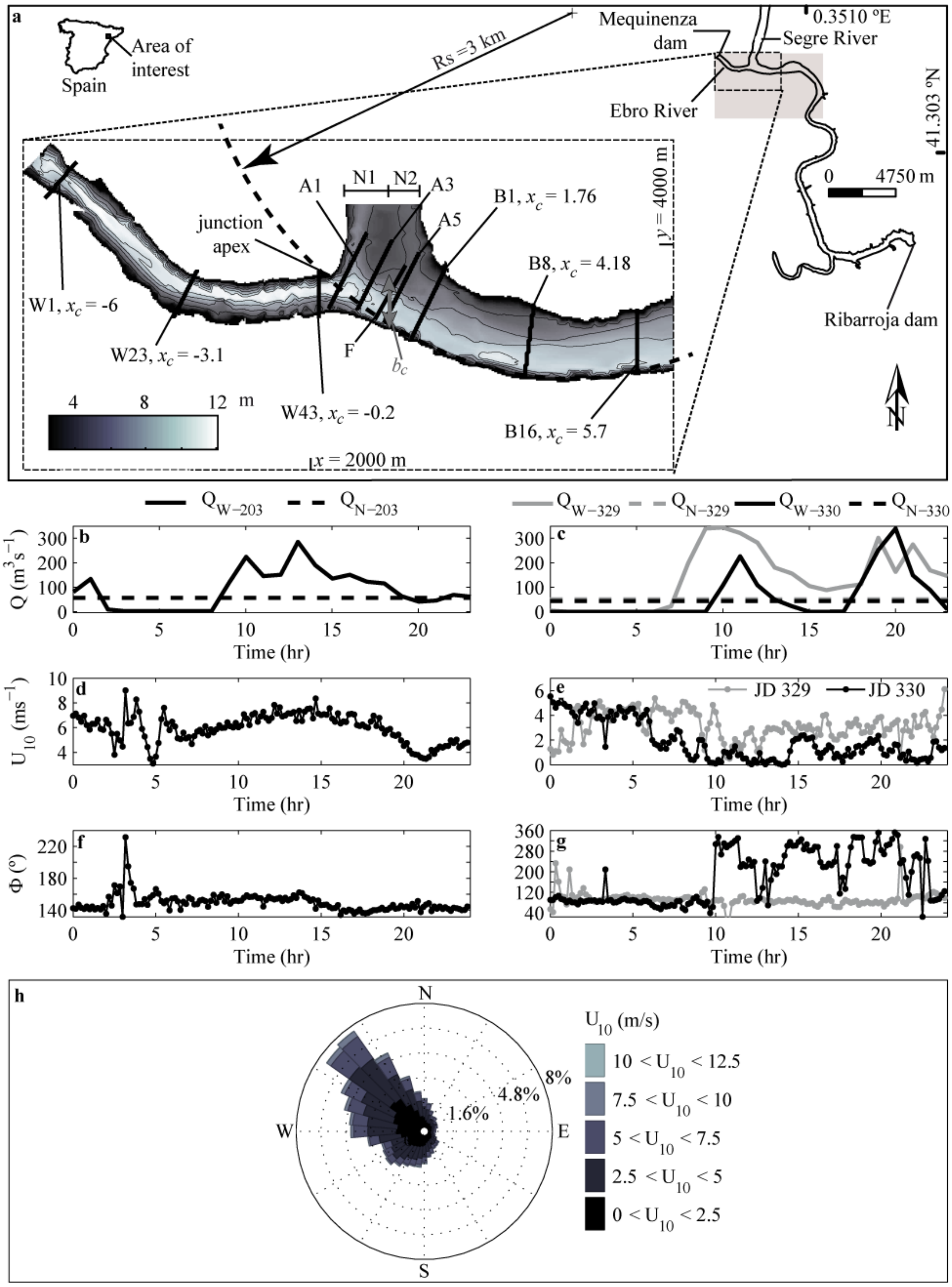

1055

1056 Figure 1

1057

1058

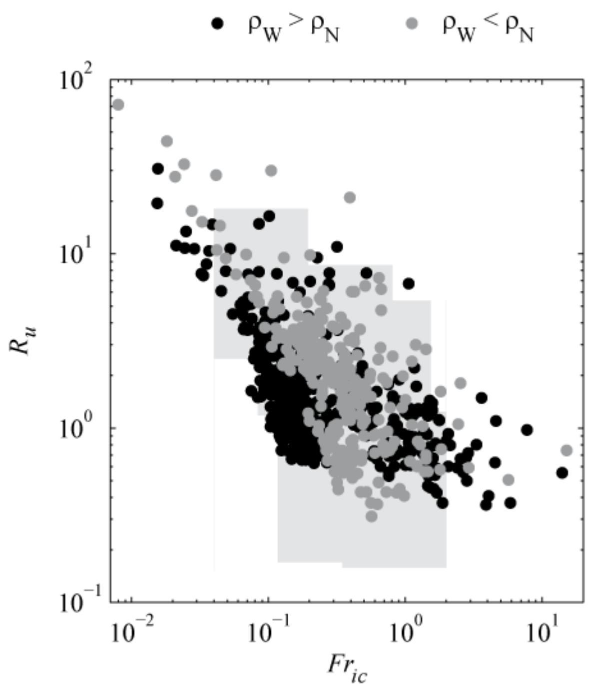

Figure 2.

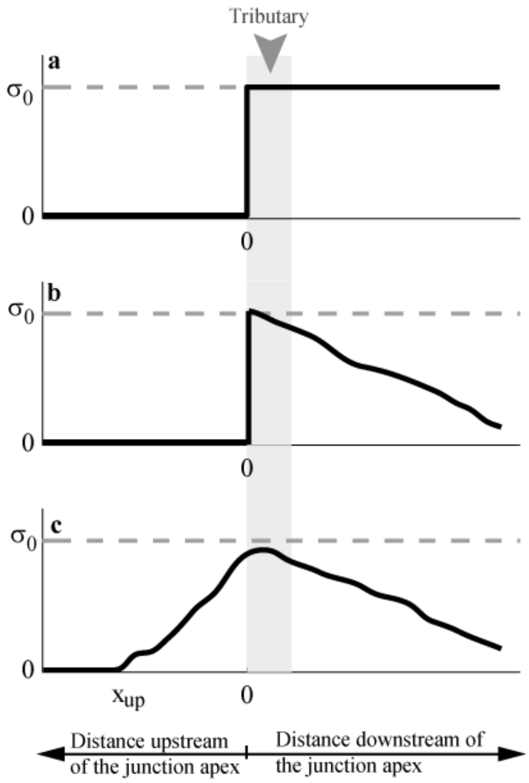
Tributary
a
b
c
σ_0
0
x_{up}
Distance upstream of the junction apex
Distance downstream of the junction apex

Figure 3

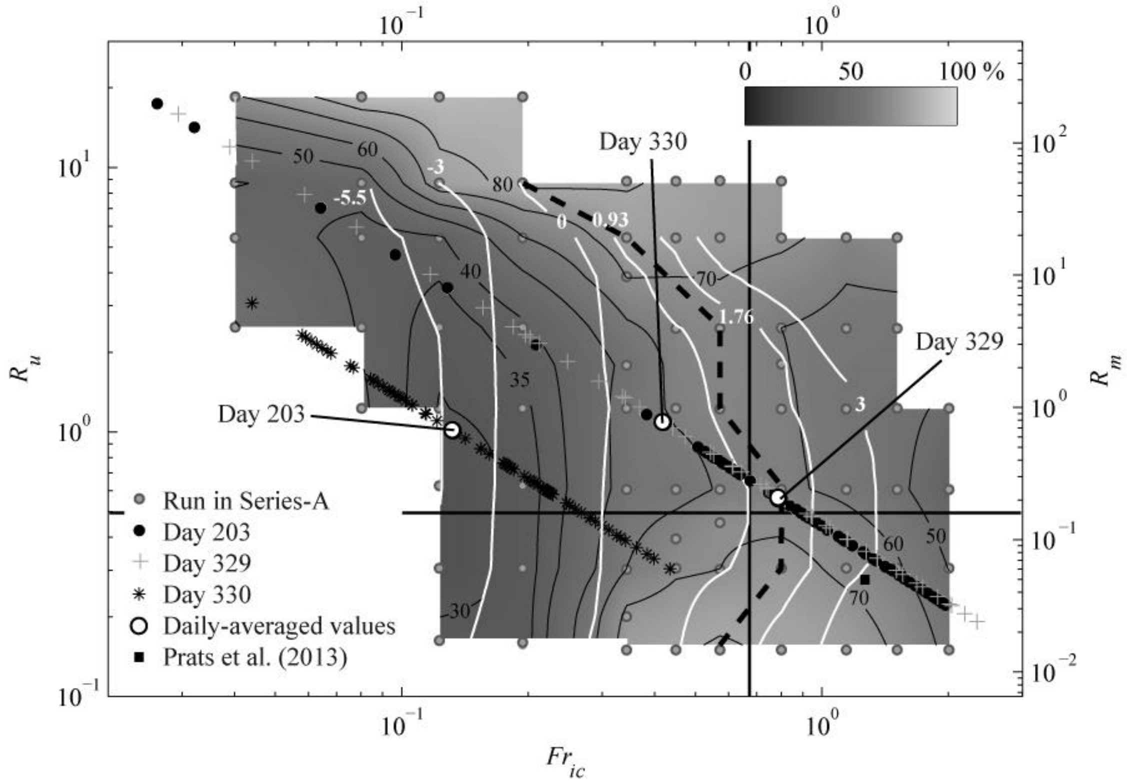

Day 330
Day 329
Day 203
0 50 100 %
Run in Series-A
Day 203
Day 329
Day 330
Daily-averaged values
Prats et al. (2013)
R_u
R_m
Fr_{ic}

Figure 4.

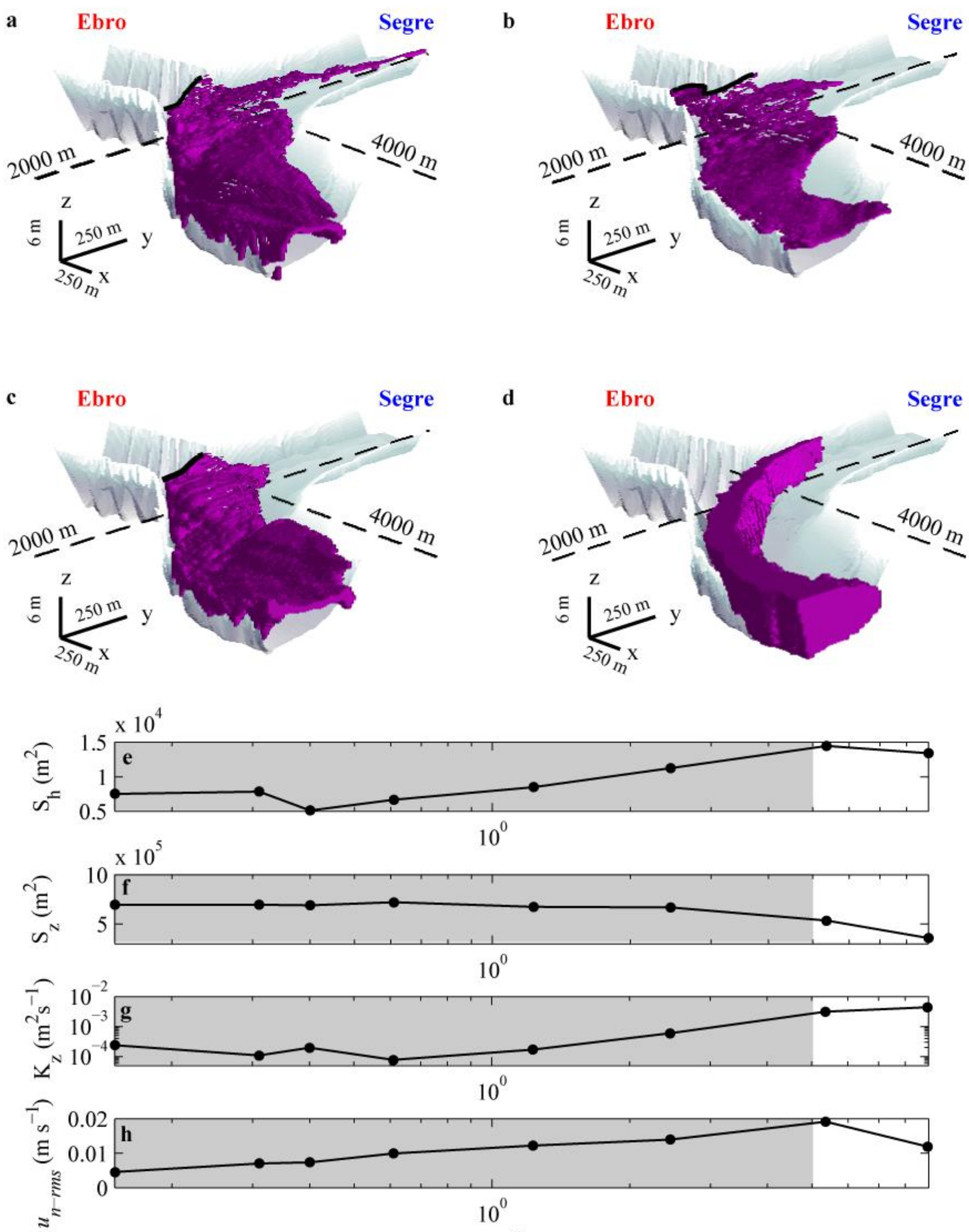
a
Ebro
Segre
2000 m
4000 m
z
6 m
250 m
y
250 m
x
b
c
d
S_h (m^2)
x 10^4
e
S_z (m^2)
x 10^5
f
K_z ($m^2 s^{-1}$)
g
u_{n-rms} (m s^{-1})
h
10^0
R_u

Figure 5.

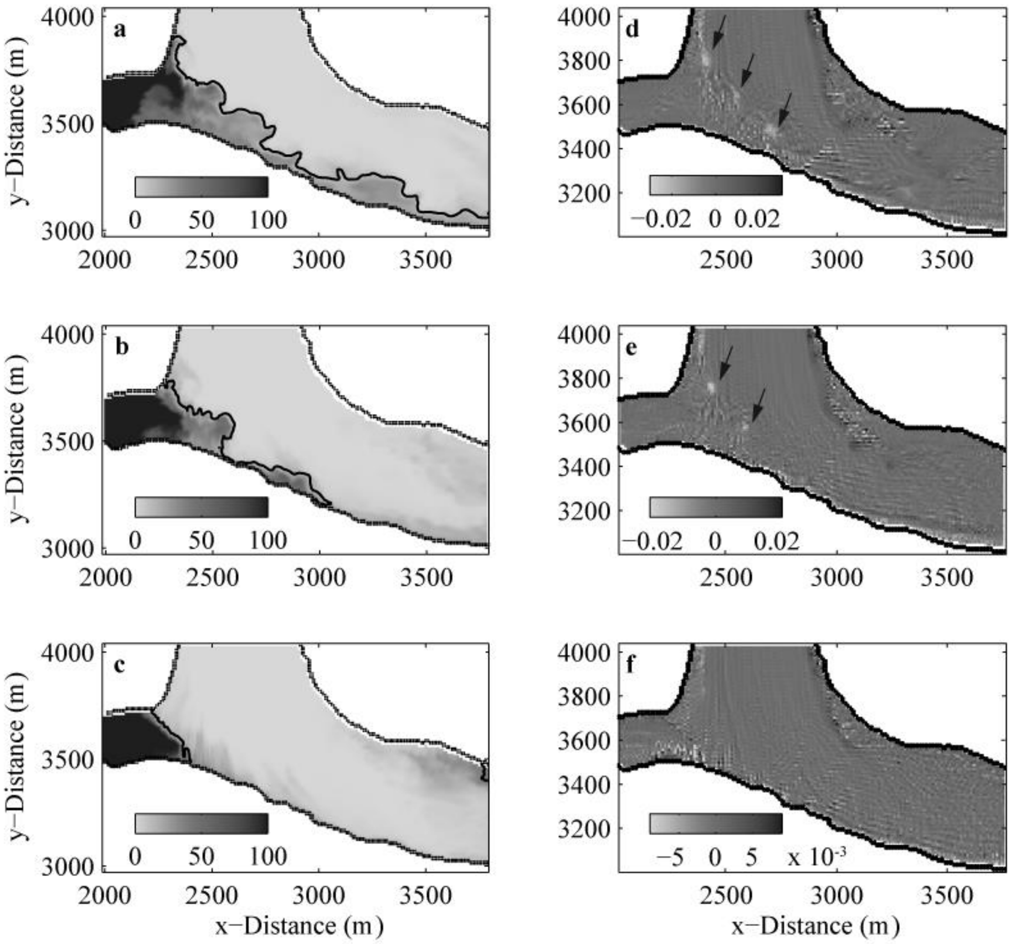
a
b
c
d
e
f
y−Distance (m)
x−Distance (m)
0 50 100
−0.02 0 0.02
−5 0 5 x 10^-3
2000 2500 3000 3500
3000 3500 4000
3200 3400 3600 3800 4000

Figure 6.

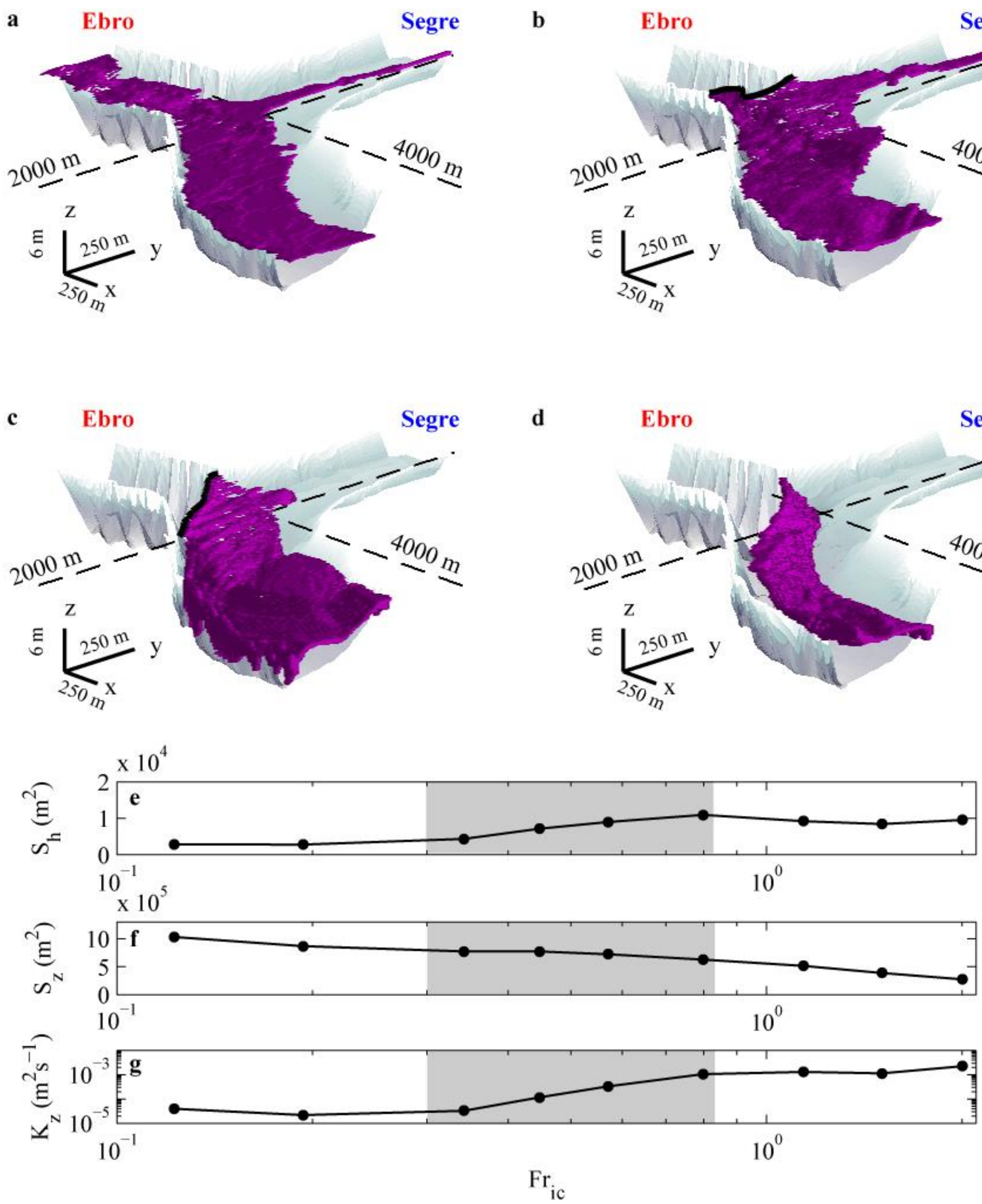
a
Ebro
Segre
2000 m
4000 m
z
y
x
6 m
250 m
250 m
b
c
d
e
f
g
x 10^4
x 10^5
S_h (m^2)
S_z (m^2)
K_z (m^2 s^-1)
Fr_ic

Figure 7.

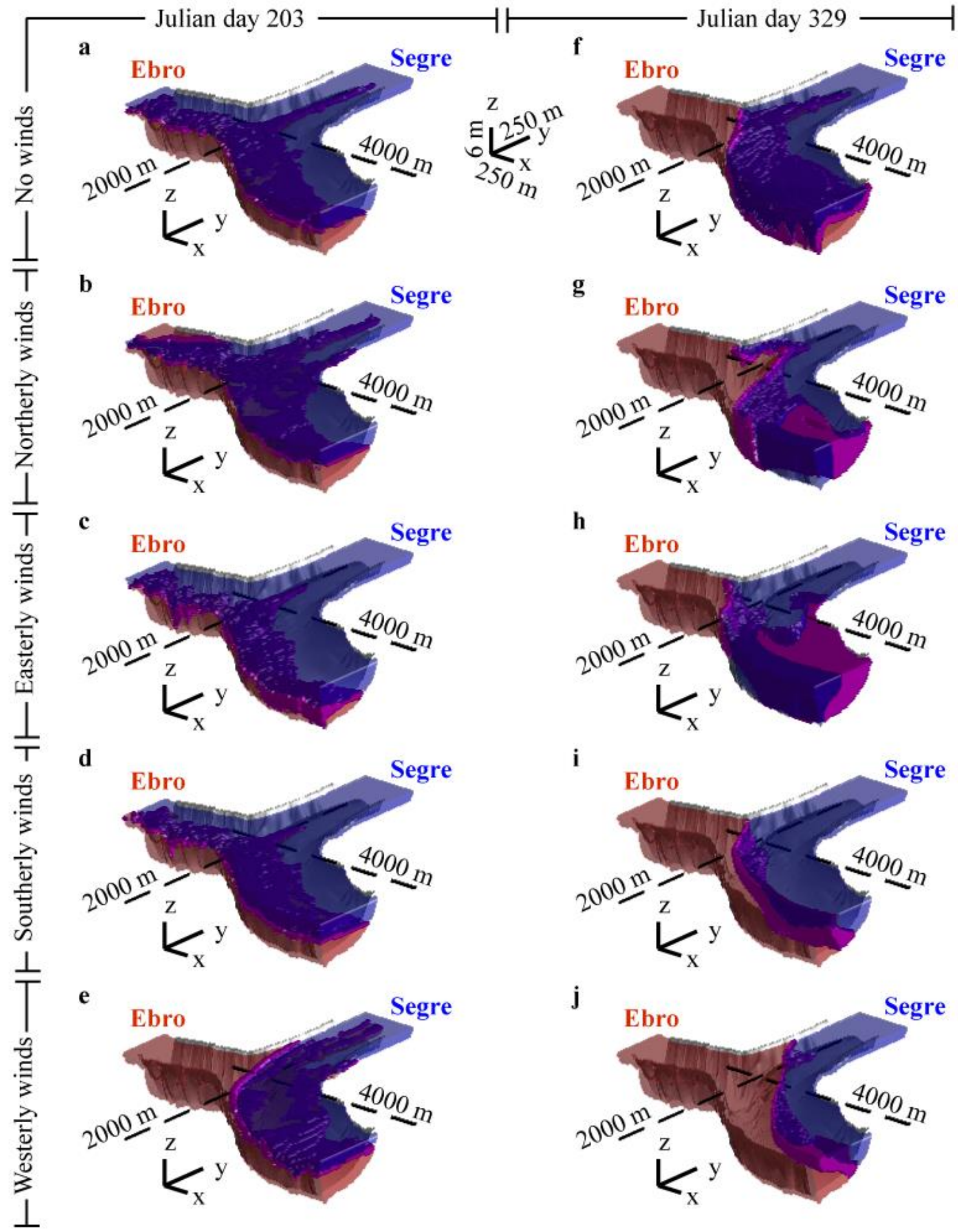
Julian day 203
Julian day 329
No winds
Northerly winds
Easterly winds
Southerly winds
Westerly winds
a
b
c
d
e
f
g
h
i
j
Ebro
Segre
2000 m
4000 m
250 m
250 m
6 m
z
y
x

Figure 8.

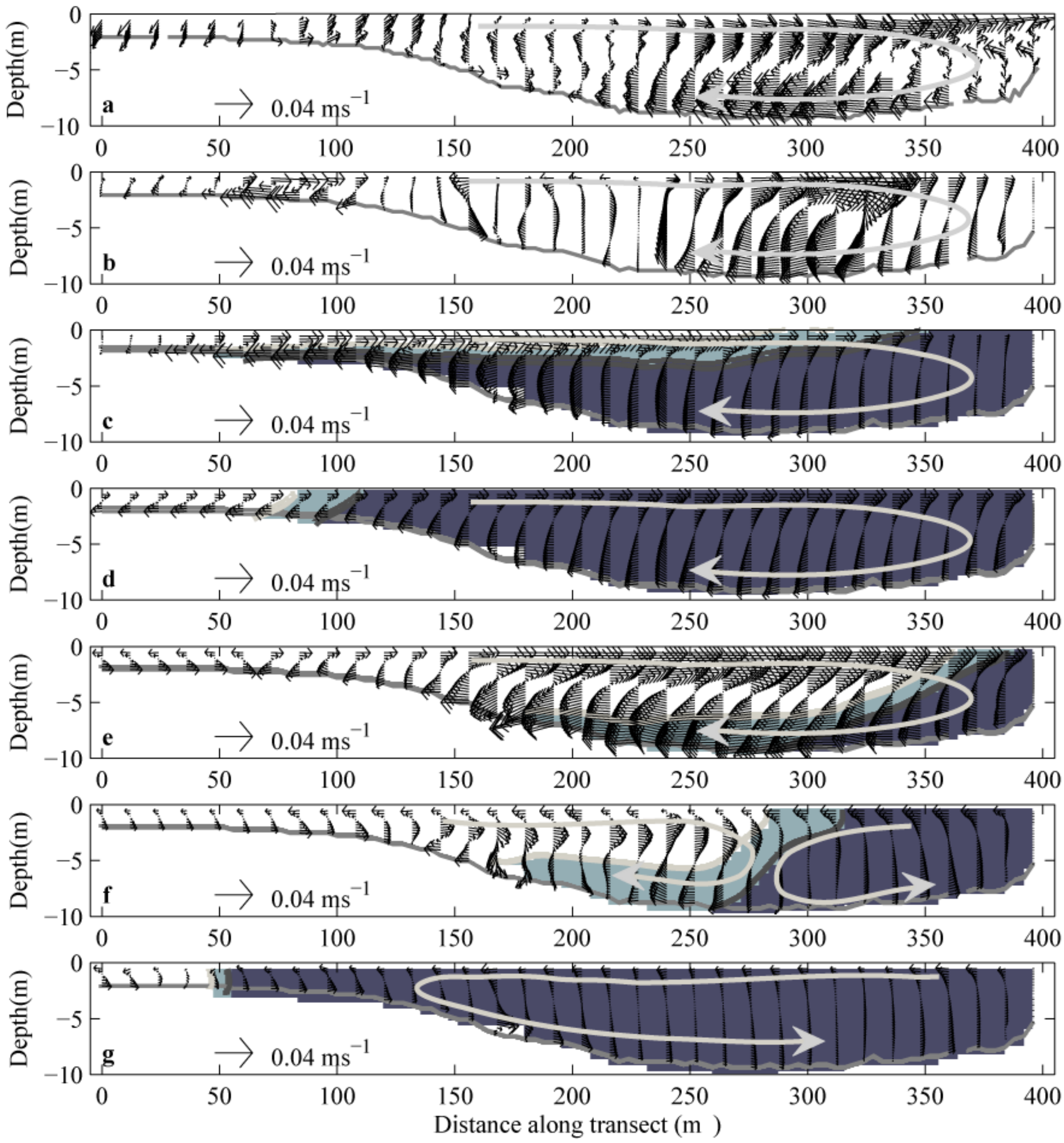
Depth(m)
0
−5
−10
a
b
c
d
e
f
g
0.04 ms^{-1}
0
50
100
150
200
250
300
350
400
Distance along transect (m)

Figure 9.

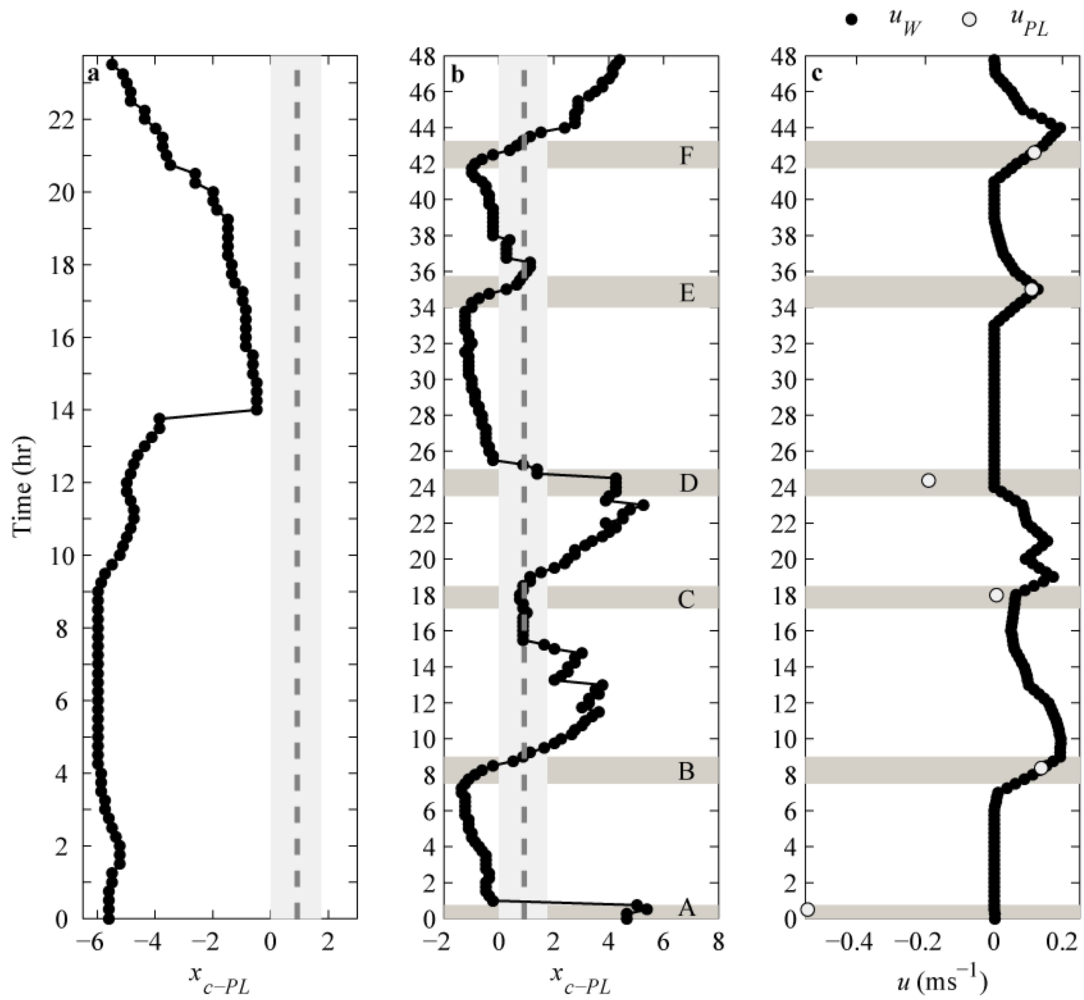

Figure 10.

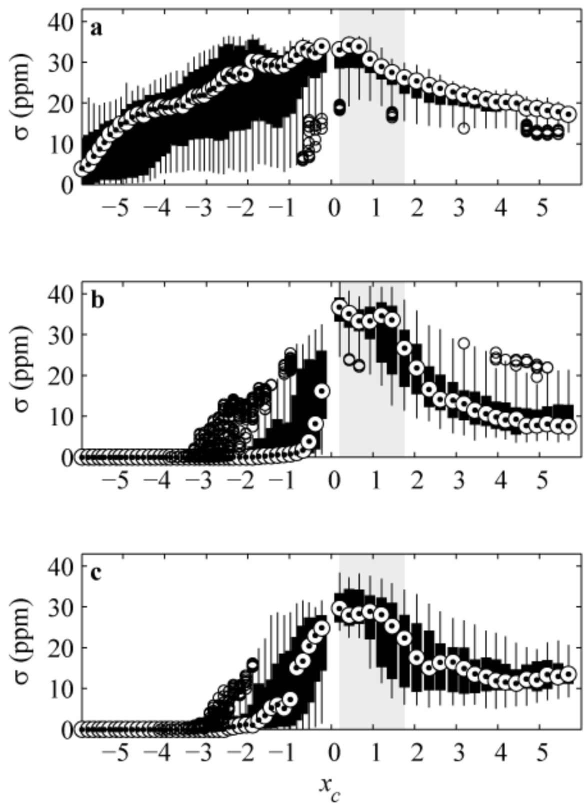

Figure 11.